NASA/TP—2006–214317

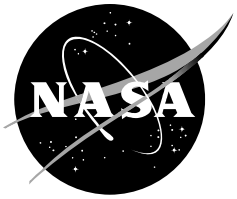

Bias Momentum Sizing for Hovering Dual-Spin Platforms

Kyong B. Lim
Langley Research Center, Hampton, Virginia

Jong-Yeob Shin
National Institute of Aerospace, Hampton, Virginia

Daniel D. Moerder
Langley Research Center, Hampton, Virginia

May 2006

NASA STI Program ... in Profile

Since its founding, NASA has been dedicated to the advancement of aeronautics and space science. The NASA scientific and technical information (STI) program plays a key part in helping NASA maintain this important role.

The NASA STI program operates under the auspices of the Agency Chief Information Officer. It collects, organizes, provides for archiving, and disseminates NASA's STI. The NASA STI program provides access to the NASA Aeronautics and Space Database and its public interface, the NASA Technical Report Server, thus providing one of the largest collections of aeronautical and space science STI in the world. Results are published in both non-NASA channels and by NASA in the NASA STI Report Series, which includes the following report types:

- TECHNICAL PUBLICATION. Reports of completed research or a major significant phase of research that present the results of NASA Programs and include extensive data or theoretical analysis. Includes compilations of significant scientific and technical data and information deemed to be of continuing reference value. NASA counterpart of peer-reviewed formal professional papers but has less stringent limitations on manuscript length and extent of graphic presentations.

- TECHNICAL MEMORANDUM. Scientific and technical findings that are preliminary or of specialized interest, e.g., quick release reports, working papers, and bibliographies that contain minimal annotation. Does not contain extensive analysis.

- CONTRACTOR REPORT. Scientific and technical findings by NASA-sponsored contractors and grantees.

- CONFERENCE PUBLICATION. Collected papers from scientific and technical conferences, symposia, seminars, or other meetings sponsored or co-sponsored by NASA.

- SPECIAL PUBLICATION. Scientific, technical, or historical information from NASA programs, projects, and missions, often concerned with subjects having substantial public interest.

- TECHNICAL TRANSLATION. English-language translations of foreign scientific and technical material pertinent to NASA's mission.

Specialized services also include creating custom thesauri, building customized databases, and organizing and publishing research results.

For more information about the NASA STI program, see the following:

- Access the NASA STI program home page at *http://www.sti.nasa.gov*

- E-mail your question via the Internet to help@sti.nasa.gov

- Fax your question to the NASA STI Help Desk at (301) 621-0134

- Phone the NASA STI Help Desk at (301) 621-0390

- Write to:
  NASA STI Help Desk
  NASA Center for AeroSpace Information
  7121 Standard Drive
  Hanover, MD 21076-1320

NASA/TP—2006–214317

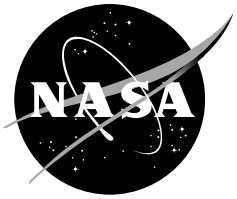

Bias Momentum Sizing for Hovering Dual-Spin Platforms

Kyong B. Lim
Langley Research Center, Hampton, Virginia

Jong-Yeob Shin
National Institute of Aerospace, Hampton, Virginia

Daniel D. Moerder
Langley Research Center, Hampton, Virginia

National Aeronautics and
Space Administration

Langley Research Center
Hampton, VA 23681

May 2006

Available from:

NASA Center for AeroSpace Information
7121 Standard Drive
Hanover, MD 21076-1320
(301) 621-0390

This report is also available in electronic form at

http://

Contents

List of Tables

List of Figures

Symbols

$\hat{b}_1, \hat{b}_3, \hat{b}_3$	unit vectors defining body-fixed frame
$(BW)_\tau$	bandwidth of external disturbance torque in roll and pitch axes
$\mathcal{B}$	axi-symmetric rigid spinning flywheel, spin axis fixed to $\mathcal{R}$
c_1, c_2	viscous damping coefficients in the roll and pitch axes respectively
$CCA(t)$	control activity defined by quadratic time integral of control vane rates
$\mathcal{E}[\cdot]$	expected value
F	unit triad $(\hat{b}_1, \hat{b}_3, \hat{b}_3)^T$ stacked as a column matrix, vectrix notation
$G(s; h_{_B})$	transfer matrix relating torques to angular velocities for roll and pitch axes
$h_{_B}$	bias angular momentum due to wheel spin Ω_B
$\underrightarrow{h}$	absolute angular momentum of $\mathcal{R}+\mathcal{B}$ about its center of mass
H_{ik}	transfer function relating kth unit disturbance torque to ith angular velocity
$\underrightarrow{I}_R$, $\underrightarrow{I}_B$	inertia dyadic of $\mathcal{R}$ and $\mathcal{B}$ respectively
I_1, I_2, I_3	principal inertia components of $\mathcal{R}+\mathcal{B}$, in F frame
I_R^1, I_R^2, I_R^3	principal inertia components of $\mathcal{R}$, in F frame
I_B^t, I_B^t, I_B^a	principal inertia components of $\mathcal{B}$, in F frame
$J(t)$	performance cost defined by time integral of attitude and position errors
O_{cm}	common center of mass for $\mathcal{R}$, $\mathcal{B}$, and $\mathcal{R}+\mathcal{B}$
$\mathcal{R}$	main rigid platform
$\mathcal{R}+\mathcal{B}$	dual-spin system
$S_{\hat{w}_i}$	PSD of ith fictitous signal, $\hat{w}_i$
S_{τ_1}, S_{τ_2}	PSD of roll and pitch disturbance torques
V	transfer function matrix of disturbance filters in roll and pitch axes
$\hat{w}$	unity norm bounded fictitious signals
x_o	frequency ratio of $(BW)_\tau$ to λ_o
β_1, β_2, β_3	vehicle attitude angles, roll-pitch-yaw
ζ, ζ_m	viscous damping ratios in roll-pitch dynamics
θ_i, $i = 1, \ldots, 4$	control vane angles
λ, λ^*	complex conjugate pair of eigenvalues associated with precession motion
λ_o	undamped precession or "Wobble" frequency
ν	frequency
ξ_1, ξ_2, ξ_3	position of vehicle (center of mass), in inertial frame
$\bar{\sigma}(\cdot)$	maximum singular value of $(\cdot)$
τ_1, τ_2	disturbance torques in roll and pitch axes
$\underrightarrow{\omega}$, $\underrightarrow{\omega}_B$	inertial angular velocity of $\mathcal{R}$ and $\mathcal{B}$ respectively
ω_1, ω_2, ω_3	roll-pitch-yaw components of the inertial angular velocity of $\mathcal{R}$, in F frame
Ω_B	spin rate of $\mathcal{B}$ relative to $\mathcal{B}$
$\|\cdot\|_2$	Euclidean norm on vector space $\mathcal{F}^n$
$\|\cdot\|_\infty$	∞-norm on vector space $\mathcal{H}_\infty$

Symbols (cont)

BM	bias momentum
LQG	linear quadratic Gaussian
MSR	mean square response
NBM	no bias momentum
DSTD	dual spin test device
PSD	power spectral density
VTOL	vertical takeoff and landing

Abstract

An atmospheric flight vehicle in hover is typically controlled by varying its thrust vector. Achieving both levitation and attitude control with the propulsion system places considerable demands on it for agility and precision, particularly if the vehicle is statically unstable, or nearly so. These demands can be relaxed by introducing an appropriately sized angular momentum bias aligned with the vehicle's yaw axis, thus providing an additional margin of attitude stability about the roll and pitch axes. This paper describes a methodical approach for trading off angular momentum bias level needed with desired levels of vehicle response due to the design disturbance environment given a vehicle's physical parameters. It also describes several simplifications that provide a more physical and intuitive understanding of dual-spin dynamics for hovering atmospheric vehicles. This approach also mitigates the need for control torques and inadvertent actuator saturation difficulties in trying to stabilize a vehicle via control torques produced by unsteady aerodynamics, thrust vectoring, and unsteady throttling. Simulation results, based on a subscale laboratory test flying platform, demonstrate significant improvements in the attitude control robustness of the vehicle with respect to both wind disturbances and off-center of gravity payload changes during flight.

1 Introduction

There has been recent interest in thrust-levitating flight vehicles capable of vertical takeoff and landing (VTOL) for reconaissance [1], [2], [3], [4], and more exotic applications such as rescue platforms for tall buildings [5], air ambulances [6], flying cars [7], and an air scooter [8]. These vehicles typically control their attitude in hover by varying their thrust vector. This requires agility and precision in controlling the thrust vector and, additionally, an adequate mathematical model of the thrust vector dynamics for designing the control law.

In spacecraft, propulsive attitude control consumes scarce expendables and can contaminate the spacecraft's instruments. Therefore, *dual-spin* stabilization is frequently preferred. Dual-spin refers to a partitioning of a body into a component that spins about an axis that is fixed in the body, and a component that remains stationary in body axes. The presence of the spinning component results in an angular momentum vector of fixed orientation for the entire system. This angular momentum bias provides a restoring moment against attitude perturbations orthogonal to the spin axis. Such passive stabilization is identical to that seen in spinning toy tops. For more detail description and discussion on dual-spin systems for spacecraft applications, namely, "gyrostat" or "bias momentum satellites", see for example, Section 6.6 in [9], Chapter 5 in [10] or Chapter 11 in [11].

For thrust-levitated vehicles, the objection to relying entirely on thrust vectoring for attitude stabilization primarily centers on the difficulty of modelling the response of the thrust vector to commands, because of unsteady fluidic phenomena. This difficulty is exacerbated when the vehicle is statically neutrally stable or unstable, since the thrust variations required for stabilization are now more active. Therefore an accurate model is needed for control law design in the presence of unsteady flow phenomena during thrust vectoring. Inclusion of a dual-spin mechanism in such vehicles, operating along the z-body axis (down), can ameliorate this difficulty by passively enhancing the stability of the vehicle, reducing the demands on the thrust vectoring system.

The disturbance environment and maneuvering envelope of thrust-levitating air vehicles is significantly different from that of spacecraft and therefore the criteria for specifying the minimum size of the dual-spin system's angular momentum bias are also different. For dual-spin spacecraft, a design practice as discussed in Section 15.3 of [9] for sizing the level of angular momentum is based on the anticipated change in the angular momentum in the system due to unknown external torques, i.e.,

$$|h_{_B}| \gg \left| \int_{t_o}^{t} \tau_{_{dist}} dt \right| \tag{1.1}$$

If the disturbance torques are cyclic in nature and the resulting perturbations are less than mission requirements, then the above passive stabilization will be adequate. However, if the disturbance torques have a non zero mean or biased trend (i.e. secular disturbances) and exceed mission attitude constraints, then active control will be additionally needed. This paper examines in detail the basic requirements and sizing of bias momentum for a generic thrust-levitating vehicle system, and the related aspects of the dynamics that govern a dual-spin system.

Section 2 briefly discuss relevant dynamics for a generic dual-spin system and introduce a *gyroscopically dominant* state that leads to analytical simplifications without explicit linearization assumptions. Section 3 examine the pitch and roll response characteristics due to pitch and roll disturances for a dual-spin system about a hovering trim condition. In particular, the precession frequency and damping for a generic dual-spin system are defined and the effect of the bias momentum level on the system response to disturbances is examined. Section 4 gives a derivation of an approximate analytical expression for the worst case response bound using maximum singular value of the frequency response matrix. Its dependence on the levels of disturbance, precession damping, and bias momentum are clearly shown. In Section 5, we examine mean square response to disturbances quantified by power spectral densities. As in Section 4, approximate analytical expressions are derived for the mean square response under various conditions. Section 6 focuses on the bias momentum sizing issue for a generic flying test platform and examines the dependence of the vehicle response on various parameters, and provides rationale for a recommended design range for bias momentum levels. Section 7 presents simulation results of the generic dual-spin vehicle under simulated wind disturbances and inertia changes during flight. The simulation includes a validation of the approximate response formulae used for bias momentum sizing. The simulation results show significant improvements in the robustness in the roll and pitch responses to large wind disturbances and inertia changes. Conclusions are given in Section 8.

2 Dynamics of a dual-spin system

Consider a dual-spin system $\mathcal{R}+\mathcal{B}$ which consists of a main rigid body platform $\mathcal{R}$, and a flywheel $\mathcal{B}$, as illustrated in Figure 1. For simplicity, let $\mathcal{R}$, $\mathcal{B}$, and $\mathcal{R}+\mathcal{B}$, be centered about

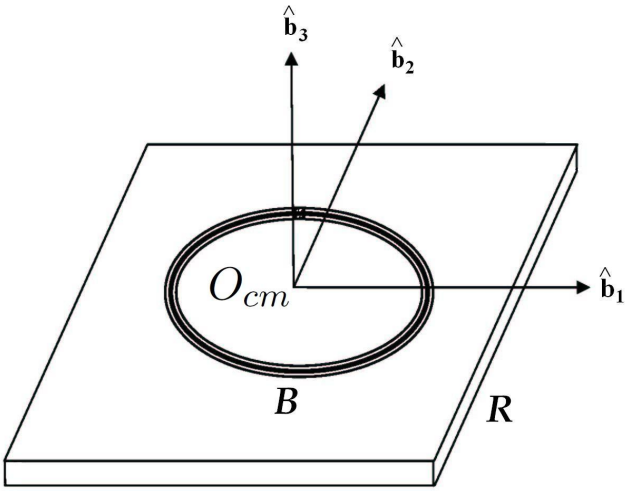

Figure 1: Schematic of a dual-spin system.

a common nominal center of mass, O_{cm}. Furthermore, using the vectrix notation in [11], let $F^T \triangleq (\hat{b}_1, \hat{b}_3, \hat{b}_3)$ denote the unit triad corresponding to the principal inertia axes for $\mathcal{R}$, $\mathcal{B}$, and $\mathcal{R}+\mathcal{B}$. In the following paragraphs, the use of the vectrix notation allows one to succiently assemble matrices of vectors and perform mathematical operations including vector operations and matrix algebra.

Let $\underset{\rightarrow}{\omega}$ denote the inertial angular velocity of $\mathcal{R}$. Suppose the flywheel, $\mathcal{B}$, is axi-symmetric with inertia dyadic, $\underset{\rightarrow}{I}_B$, and spins at a rate Ω_B with respect to the main platform, $\mathcal{R}$, with inertia $\underset{\rightarrow}{I}_R$, along its $\hat{b}_3$ axis which is fixed in $\mathcal{R}$. Hence, the inertial angular velocity of $\mathcal{B}$, can be written as $\underset{\rightarrow}{\omega}_B \triangleq \underset{\rightarrow}{\omega} + \Omega_B \hat{b}_3$. The angular momentum of $\mathcal{R}+\mathcal{B}$ about its center of mass can then be written as

$$\underset{\rightarrow}{h} = \underset{\rightarrow}{I}_R \cdot \underset{\rightarrow}{\omega} + \underset{\rightarrow}{I}_B \cdot \underset{\rightarrow}{\omega}_B \tag{2.1}$$

By defining the net external torque disturbance on $\mathcal{R}+\mathcal{B}$ about its center of mass as

$$\underset{\rightarrow}{\tau} = F^T \tau, \quad \tau \triangleq \left\{ \begin{array}{c} \tau_1 \\ \tau_2 \\ \tau_3 \end{array} \right\} \tag{2.2}$$

the rotational equations of motion for $\mathcal{R}+\mathcal{B}$ in vector form

$$\underset{\rightarrow}{\tau} = \dot{\underset{\rightarrow}{h}} = \frac{d}{dt}\left(\underset{\rightarrow}{h}\right)_F + \underset{\rightarrow}{\omega} \times \underset{\rightarrow}{h} \tag{2.3}$$

can be expressed in the following scalar form

$$\tau_1 = I_1\dot{\omega}_1 + \omega_2\left[h_{_B} + \omega_3(I_3 - I_2)\right] \tag{2.4}$$
$$\tau_2 = I_2\dot{\omega}_2 - \omega_1\left[h_{_B} + \omega_3(I_3 - I_1)\right] \tag{2.5}$$
$$\tau_3 = I_3\dot{\omega}_3 + \dot{h}_B + (I_2 - I_1)\omega_1\omega_2 \tag{2.6}$$

where the following inertia dyadics and vectors are expressed in principal inertia coordinates, as follows:

$$\underrightarrow{I} \triangleq \underrightarrow{I}_R + \underrightarrow{I}_B = F^T I F, \quad \text{where } I \triangleq \text{diag}\,(I_1, I_2, I_3) = I_R + I_B \tag{2.7}$$
$$\underrightarrow{I}_B \triangleq F^T I_B F, \quad \text{where } I_B \triangleq \text{diag}\left(I_B^t, I_B^t, I_B^a\right) \tag{2.8}$$
$$\underrightarrow{I}_R \triangleq F^T I_R F, \quad \text{where } I_R \triangleq \text{diag}\left(I_R^1, I_R^2, I_R^3\right) \tag{2.9}$$
$$\underrightarrow{\omega} \triangleq F^T\omega, \quad \text{where } \omega \triangleq \left\{\begin{array}{c}\omega_1\\ \omega_2\\ \omega_3\end{array}\right\} \tag{2.10}$$
$$\underrightarrow{h}_B \triangleq F^T\left\{\begin{array}{c}0\\ 0\\ h_{_B}\end{array}\right\} \quad \text{where } h_{_B} \triangleq I_B^a\Omega_B \tag{2.11}$$

Note that if the angular momentum of flywheel due to its spin, $h_{_B}$, is zero, then the above dual-spin dynamical equations 2.4 to 2.6 reduces to the familiar Euler equations describing the attitude dynamics for a single rigid body (see for example [12], [13]). The terms, $\omega_2 h_{_B}$ and $\omega_1 h_{_B}$, appearing in the roll (1-axis) and pitch (2-axis) equations 2.4 and 2.5, represent the internal gyroscopic torques due to the bias momentum in the flywheel. Clearly, these internal gyroscopic torques can be made to "dominate" the motion with a sufficiently large angular momentum in the dual-spin system. Notice in equation 2.6 that a similar bias momentum induced gyroscopic torque does not appear in the yaw axis, rather, the reaction torque, $\dot{h}_B$, due to an angular acceleration of the flywheel appears. It is well known that the presence (and absence) of the bias momentum induced gyroscopic torques in the roll and pitch axes (in yaw axis) gives rise to the directional stability (unrestrained motion) in the roll and pitch axes.

Suppose the flywheel spins at a constant rate

$$|\dot{h}_B| = 0 \tag{2.12}$$

and the bias momentum in the flywheel dominates in the following sense:

Definition 1 *The dual-spin dynamical system defined by equations 2.4 to 2.6 is said to be a "gyroscopically dominant" state if*

$$|h_{_B}| \gg \max\left(|(I_3 - I_2)|, |(I_3 - I_1)|\right) \cdot |\omega_3| \tag{2.13}$$

Then, the dynamics of this generic dual spin system can be approximated by

$$I_1\dot{\omega}_1 \approx -\omega_2 h_{_B} + \tau_1 \tag{2.14}$$
$$I_2\dot{\omega}_2 \approx \omega_1 h_{_B} + \tau_2 \tag{2.15}$$
$$I_3\dot{\omega}_3 = -(I_2 - I_1)\omega_1\omega_2 + \tau_3 \tag{2.16}$$

Alternately, if the dual spin equations in 2.4 to 2.6 are linearized about angular velocities of $\omega_i = 0$ by assuming $|\omega_i| \ll 1$, for $i = 1, 2, 3$, the following results

$$I_1\dot{\omega}_1 \approx -\omega_2 h_{_B} + \tau_1 \tag{2.17}$$

$$I_2\dot{\omega}_2 \approx \omega_1 h_{_B} + \tau_2 \tag{2.18}$$

$$I_3\dot{\omega}_3 \approx \tau_3 \tag{2.19}$$

Notice that the roll and pitch dynamics arrived at by bias momentum dominance, as given by equations 2.14 and 2.15, are identical to the corresponding linearized equations 2.17 and 2.18. However, the yaw dynamics are different in that equation 2.16 is an exact nonlinear equation while equation 2.19 is an approximate linear equation.

In summary, as long as a dual-spin system is *gyroscopically dominant*, i.e., equation 2.13 is valid, the *linear* roll and pitch dynamics, as given by equations 2.14 to 2.16, will be valid without having to assume small "linear" angular velocity motion. On the other hand, if the bias momentum level in the dual-spin system is such that it is not *gyroscopically dominant*, then linearity assumptions must be made in order for linear equations 2.14 and 2.15 to hold.

3 Pitch-Roll Dynamics about Trim

As evident in equations 2.14 and 2.15, the roll and pitch states, ω_1 and ω_2, are independent of the yaw state, ω_3, although the pitch and roll nonlinear gyroscopic term, $(I_2-I_1)\omega_1\omega_2$ influences yaw motion directly. With this fact, consider only the following linear roll and pitch dynamics from equations 2.14 and 2.15

$$\left\{ \begin{array}{c} \dot{\omega}_1 \\ \dot{\omega}_2 \end{array} \right\} \approx A \left\{ \begin{array}{c} \omega_1 \\ \omega_2 \end{array} \right\} + B \left\{ \begin{array}{c} \tau_1 \\ \tau_2 \end{array} \right\} \tag{3.1}$$

where

$$A \triangleq \left[\begin{array}{cc} -\frac{c_1}{I_1} & -\frac{h_B}{I_1} \\ \frac{h_B}{I_2} & -\frac{c_2}{I_2} \end{array} \right], \quad B \triangleq \left[\begin{array}{cc} I_1^{-1} & 0 \\ 0 & I_2^{-1} \end{array} \right] \tag{3.2}$$

Notice from the diagonal elements of the system matrix A in equation 3.2 that the viscous damping terms c_1 and c_2 have been added. These terms are intended to represent the physical energy dissipation mechanism during the precession/nutation motion which are described by their respective angular velocities of ω_1, and ω_2. For example, the energy dissipation associated with a "wobble" or "nutation" damper (see for example [14]), whether implemented passively or actively, can be accounted using the above viscous damper model. Although in general, damping or energy dissipation effects for a particular physical system are difficult to model accurately, in this study, these parameters are used in the limited context of a performance trade study for the purpose of momentum wheel sizing.

In transfer function form, the above roll and pitch dynamics can be expressed as

$$\left\{ \begin{array}{c} \omega_1 \\ \omega_2 \end{array} \right\} = G(s;h_{_B}) \left\{ \begin{array}{c} \tau_1 \\ \tau_2 \end{array} \right\} \tag{3.3}$$

where

$$G(s;h_{_B}) = \frac{1}{\Delta(s)} \left[\begin{array}{cc} \frac{s}{I_1} + \frac{c_2}{I_1 I_2} & -\frac{h_B}{I_1 I_2} \\ \frac{h_B}{I_1 I_2} & \frac{s}{I_2} + \frac{c_1}{I_1 I_2} \end{array} \right]; \quad \Delta(s) \triangleq (s-\lambda)(s-\lambda^*) \tag{3.4}$$

with the complex conjugate eigenvalue pair

$$\lambda, \lambda^* = -\zeta\omega_o \pm j\omega_o\sqrt{1-\zeta^2} \tag{3.5}$$

and

$$\zeta \triangleq \frac{1}{2\omega_o}\left(\frac{c_1}{I_1}+\frac{c_2}{I_2}\right) = \frac{1}{\sqrt{1+\frac{c_1 c_2}{h_B^2}}}\zeta_m, \quad \zeta_m \triangleq \frac{1}{2}\left[\sqrt{\frac{I_2}{I_1}}\left(\frac{c_1}{h_{_B}}\right)+\sqrt{\frac{I_1}{I_2}}\left(\frac{c_2}{h_{_B}}\right)\right] \tag{3.6}$$

$$\omega_o \triangleq \lambda_o\sqrt{1+\frac{c_1 c_2}{h_B^2}} \tag{3.7}$$

$$\lambda_o \triangleq \frac{h_{_B}}{\sqrt{I_1 I_2}} \tag{3.8}$$

The transfer function matrix $G(s;h_{_B})$ defines the roll and pitch angular velocity frequency response to external roll-pitch torque disturbances. The complex conjugate pair of eignevalues

in equation 3.5 corresponds to the often dominant precession motion due to the bias momentum induced gyroscopic coupling in the roll and pitch axes. This eigenvalue pair is parameterized in the familiar form for a second order oscillatory system involving damping ratio, ζ, and frequency, ω_o, given by equations 3.6 and 3.7, respectively. The term λ_o as given in equation 3.8 denotes the undamped precession or wobbling frequency of oscillation and is analogous to the precession frequency in a dual-spin spacecraft as described for example in Chapter 6 of [11]. Notice from equation 3.7 that the damped frequency, ω_o, reduces to this precession frequency, λ_o, in the absence of damping, i.e., $\zeta = 0$. This precession frequency increases linearly with the level of bias momentum and is inversely proportional to the rotational inertia of the vehicle.

Defining the following special forms for the damping ratio, ζ, as given in equation 3.6, will lend clarity in the following paragraphs:

$$\zeta = \frac{\frac{c}{h_{_B}}}{\sqrt{1+\left(\frac{c}{h_{_B}}\right)^2}} \frac{1}{2}\left[\sqrt{\frac{I_2}{I_1}}+\sqrt{\frac{I_1}{I_2}}\right] \qquad \text{if } c_1 = c_2 = c \tag{3.9}$$

$$= \frac{\frac{c}{h_{_B}}}{\sqrt{1+\left(\frac{c}{h_{_B}}\right)^2}} \qquad \text{if } c_1 = c_2 = c, \text{ and } I_1 = I_2 = I \tag{3.10}$$

$$\approx \frac{c}{h_{_B}} \qquad \text{if } c_1 = c_2 = c,\ I_1 = I_2 = I, \text{ and } |c/h_{_B}| \ll 1 \tag{3.11}$$

Notice from equation 3.11 that for "small" damping, the ratio, $\zeta_m = \frac{c}{h_{_B}}$, can be assumed to be the damping ratio in the system.

Figure 2 shows the log magnitudes of the roll and pitch angular velocity responses to corresponding disturbance torques, at bias momentum levels of $(0, .1, 1, 10, 50)$ Nms. Small damping constants corresponding to $c_1 = c_2 = 0.02h_{_B}$ are assumed in the above figures, corresponding to about 2 percent damping ratios for each case. The case with $h_{_B} = 0$ is shown by dashed lines in the figure. Note that there are no dashed lines in the off-diagonal plots since there is no coupling in roll and pitch. In all the subplots in Figure 2, notice that the responses decrease and their peaks shift to higher frequencies, with increasing bias momentum levels. Notice that increasing the level of bias momentum can significantly reduce the roll and pitch angular velocity response to disturbances. Furthermore, as the level of bias momentum increases, the roll response to roll disturbances decreases more rapidly than the roll response to pitch disturbances. Alternately, the dynamically uncoupled system at zero bias momentum transforms to a system whose characteristic dynamics are *gyroscopically dominant* (see definition in equation 2.13).

Based on equation 3.3, Figure 3 shows the maximum singular value frequency response of the roll and pitch angular velocities, and is given as follows

$$\bar{\sigma}\left[G(j\nu; h_{_B})\right] = \sup_{\tau} \frac{\|\omega(j\nu)\|_2}{\|\tau(j\nu)\|_2}, \quad \forall \nu \tag{3.12}$$

where $\tau \triangleq (\tau_1, \tau_2)$, $\omega \triangleq (\omega_1, \omega_2)$, and $\|\cdot\|_2$ denotes the Euclidean norm on $\mathcal{F}^n$. If the above

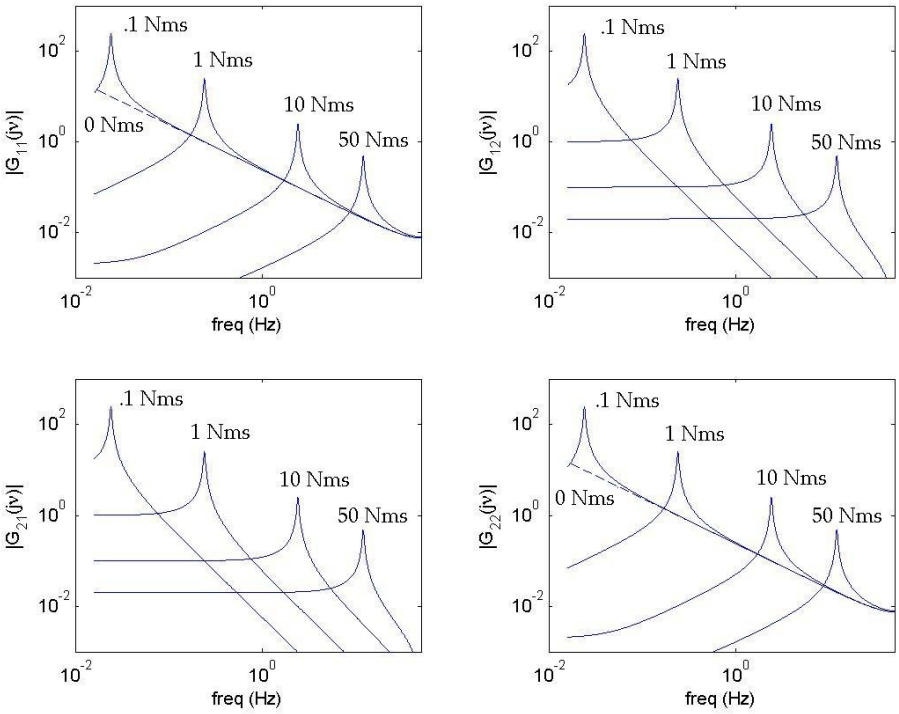

Figure 2: Roll and pitch angular velocity responses to roll and pitch disturbance torques for bias momentum levels of (0, .1, 1, 10, 50) Nms; $c_1/h_B = c_2/h_B = 0.02$.

supremum of Eulidean norm ratio is searched for the worst case over all frequencies,

$$\max_{\nu} \bar{\sigma}\left[G(j\nu; h_{_B})\right] = \|G(j\nu; h_{_B})\|_{\infty} \tag{3.13}$$

then the above H_{∞} norm can also be expressed in terms of induced signal 2-norms (see for example [15], [16]). The maximum singular value captures the directionally worst case response

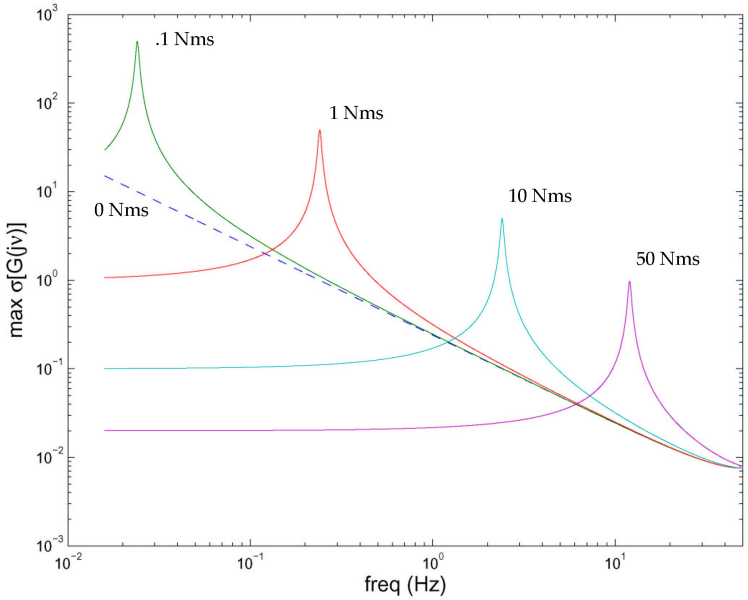

Figure 3: Maximum singular value angular velocity responses to roll and pitch disturbance torques for bias momentum levels of (0, .1, 1, 10, 50) Nms; $c_1/h_{_B} = c_2/h_{_B} = 0.02$.

due to simultaneous disturbance torques in roll and pitch. In both figures, the dashed line represents the reference case with near zero bias momentum. As in the previous plots, the responses shown in Figure 3 decrease and their peaks shift to higher frequencies, with increasing bias momentum levels. Notice from the maximum singular value frequency response that it looks similar to an undamped second order system with a resonance peak at the precession frequency given by equation 3.5.

The next two sections consider two bias momentum sizing approaches for the generic dual-spin system which are based on the angular velocity responses of the main platform to a set of disturbances. These approaches differ in their assumptions in the disturbances and the metric used to describe the roll-pitch responses. As will be evident, various simplifying assumptions are made to obtain corresponding intuitive analytical expressions for responses which are only approximate but nevertheless useful for sizing and conceptual design of effective bias momentum levels.

4 Worst Case Response Bound

4.1 Disturbance Model

In this approach to sizing, assume that the external disturbances are unknown but bounded and can be expressed as

$$\tau = V(j\nu)\hat{w} \tag{4.1}$$

where $V(j\nu) \in \mathcal{C}^{2\times 2}$ denotes a frequency response matrix representation of a filter, which is driven by an unknown fictitious source signal vector, $\hat{w} \in \mathcal{C}^{2\times 1}$, which is assumed to be unity bounded as follows

$$\|\hat{w}(j\nu)\|_2 \leq 1, \quad \forall\nu \tag{4.2}$$

Suppose τ_1 and τ_2 are independent disturbance signals having a flat frequency response over a bandwidth, $(BW)_\tau$. Hence, from equations 4.1 and 4.2, the magnitude of the disturbance filter can be approximated as follows

$$|V_{ik}(j\nu)| = \frac{|\tau_i(j\nu)|}{|\hat{w}_k(j\nu)|} \approx \begin{cases} a_i, & i = k \\ 0, & i \neq k \end{cases} \quad \forall\nu < (BW)_\tau, \;\; i,k = 1,2 \tag{4.3}$$

and the disturbance filter is assumed to roll-off rapidly outside the bandwidth.

4.2 Static Approximation

The frequency response matrix from equations 3.4 and 4.3 can be written as

$$G(j\nu; h_{_B})V(j\nu) = \frac{1}{\Delta(j\nu)} \begin{bmatrix} (\frac{j\nu}{I_1} + \frac{c_2}{I_1 I_2})V_{11} & -\frac{h_{_B}}{I_1 I_2}V_{22} \\ \frac{h_{_B}}{I_1 I_2}V_{11} & (\frac{j\nu}{I_2} + \frac{c_1}{I_1 I_2})V_{22} \end{bmatrix} \tag{4.4}$$

where $\Delta(j\nu)$ denotes the value of $\Delta(s)$ as defined in equation 3.4 but evaluated at $s = j\nu$. Based on the maximum singular value frequency response given by equation 3.12 and plotted in Figure 3, the following approximations are considered

$$\bar{\sigma}\left[G(j\nu; h_{_B})\right] \approx \bar{\sigma}\left[G(0; h_{_B})\right], \quad \text{for } \nu < \lambda_o \tag{4.5}$$

Since $V(j\nu)$ is assumed to be diagonal with constant frequency responses as described in equation 4.3 over a certain bandwidth, $(BW)_\tau$, it follows that over frequency, ν, where

$$\nu : \nu < (BW)_\tau < \lambda_o \tag{4.6}$$

the maximum singular value frequency response can be approximated by the following static approximations:

$$\begin{aligned}
\bar{\sigma}\left[G(j\nu;h_{_B})V(j\nu)\right] &\approx \bar{\sigma}\left[G(0;h_{_B})V(0)\right] \\
&= \frac{1}{h_{_B}(1+\frac{c_1c_2}{h_{_B}^2})}\bar{\sigma}\begin{bmatrix} \frac{c_2}{h_{_B}}V_{11} & -V_{22} \\ V_{11} & \frac{c_1}{h_{_B}}V_{22} \end{bmatrix} && (4.7)\\
&= \frac{1}{h_{_B}\sqrt{1+\frac{c_1c_2}{h_{_B}^2}}}\max\left(\sqrt{D+\sqrt{D^2-E}},\ \sqrt{D-\sqrt{D^2-E}}\right) && (4.8)\\
&= \frac{1}{h_{_B}\sqrt{1+\left(\frac{c}{h_{_B}}\right)^2}}\max\left(|V_{11}|,|V_{22}|\right), \quad \text{if } c_1=c_2=c && (4.9)
\end{aligned}$$

where

$$\begin{aligned}
D &\triangleq \frac{1}{2}\left[\frac{1+\left(\frac{c_2}{h_{_B}}\right)^2}{1+\frac{c_1c_2}{h_{_B}^2}}\right]V_{11}^2+\frac{1}{2}\left[\frac{1+\left(\frac{c_1}{h_{_B}}\right)^2}{1+\frac{c_1c_2}{h_{_B}^2}}\right]V_{22}^2 && (4.10)\\
E &\triangleq V_{11}^2V_{22}^2 && (4.11)
\end{aligned}$$

Notice that with the additional assumption in the damping constants satisfying the relations $c_2 = c_1 = c$, the response formula simplifies considerably to equation 4.9. Furthermore, if the system is undamped or is only lightly damped, i.e.,

$$c_1/h_{_B} \ll 1 \quad \text{and} \quad c_2/h_{_B} \ll 1 \qquad \text{or} \qquad c/h_{_B} \ll 1 \tag{4.12}$$

then the damping term can be completely ignored, simplifying even further.

Consider bounding the maximum frequency response of the roll and pitch angular velocities given a bounded set of disturbance torques as described in equations 4.2 and 4.3. The roll-pitch angular velocity response from equations 3.3 and 4.1 is

$$\omega(j\nu) = G(j\nu;h_{_B})V(j\nu)\hat{w}(j\nu) \tag{4.13}$$

Based on the worst case response at each frequency, as given in equation 4.9, quantify the above frequency response bound requirement approximately as follows

$$\sup_{\hat{w}}\|\omega(j\nu)\|_2 = \bar{\sigma}\left[G(j\nu;h_{_B})V(j\nu)\right] \approx \frac{\max\left(|V_{11}|,|V_{22}|\right)}{h_{_B}\sqrt{1+\left(\frac{c}{h_{_B}}\right)^2}} < \|\omega_{target}(\nu)\|_2 \tag{4.14}$$

The term $\|\omega_{target}(\nu)\|_2$ denotes a maximum desirable angular velocity response at the frequency of interest, ν.

5 Mean Square Response Bound

In this alternate approach, consider the mean square response (MSR) in the roll and pitch angular velocities given that the disturbance torques are random processes with known power spectral densities (PSD).

5.1 Disturbance Model

The disturbance filter model in equation 4.1 is assumed except that a different meaning is attributed to the fictitious signal $\hat{w}$, assumed now to be a unit white noise process so that its PSD for $i = 1, 2$, is

$$S_{\hat{w}_i}(\nu) = 1, \quad \forall \nu \tag{5.1}$$

As in the previous approach, assume that the disturbance torques, τ_1, and τ_2 are independent and have a near constant spectral density over a certain bandwidth, $(BW)_\tau$. This means that the disturbance filter is diagonal and has the same form as described in equation 4.3.

With the above unit white noise driven disturbance torque model, since their PSD's are related by

$$S_{\tau_i}(\nu) = |V_{ii}(j\nu)|^2 S_{\hat{w}_i}(\nu) \tag{5.2}$$

the frequency response magnitude corresponding to equation 4.3 is

$$|V_{ik}(j\nu)| = \frac{|\tau_i(j\nu)|}{|\hat{w}_k(j\nu)|} \approx \begin{cases} \sqrt{S_{\tau_i}(\nu)}, & i = k \\ 0, & i \neq k \end{cases} \quad \forall \nu < (BW)_\tau, \; i, k = 1, 2 \tag{5.3}$$

Analogously, assume that the disturbance torque PSD rolls-off rapidly beyond a certain bandwidth, $(BW)_\tau$.

Suppose the PSD of the anticipated disturbance torques, $S_{\tau_1}(j\nu)$ and $S_{\tau_2}(j\nu)$, can be approximated by constants, $S^o_{\tau_1}$ and $S^o_{\tau_2}$, over a bandwidth, BW_τ, as given in equation 4.6 and rolls-off rapidly beyond, BW_τ. For instance, in dealing with gust loads on aircraft, Von Karman and Dryden gust velocity PSD's are used widely in design and simulation. These spectra basically approximate flat, low pass filters whose parameters depend on various flight conditions such as nominal airspeed and altitude. The break frequencies for these well known gust PSD's are low (for example .1 to 1 Hertz) and they roll-off at orders 5/3 and 2 respectively (see for example [17]). These assumptions on the gust PSD structure lead to the following simplifying formulae for the mean square torque

$$\mathcal{E}[\tau^T \tau] \approx 2(S^o_{\tau_1} + S^o_{\tau_2})(BW)_\tau \tag{5.4}$$

5.2 Static Approximation

For the system given in equation 4.13, the response PSD for the roll-pitch angular velocities can be expressed as [18]

$$S_\omega(\nu) = \left\{ \begin{array}{c} S_{\omega_1}(\nu) \\ S_{\omega_2}(\nu) \end{array} \right\} = \left[\begin{array}{cc} |H_{11}|^2 & |H_{12}|^2 \\ |H_{21}|^2 & |H_{22}|^2 \end{array} \right] \left\{ \begin{array}{c} S_{\hat{w}_1}(\nu) \\ S_{\hat{w}_2}(\nu) \end{array} \right\} \tag{5.5}$$

where

$$H_{ik}(j\nu) \triangleq [G(j\nu; h_{_B})V(j\nu)]_{ik} \tag{5.6}$$

denotes the (i,k) frequency response from kth-white noise disturbance torque to ith-angular velocity of vehicle. The mean square response of the ith-angular velocity response can be obtained from the response spectra given in equation 5.5 as

$$\mathcal{E}[\omega_i^2] = \int_{-\infty}^{\infty} \sum_{k=1}^{2} |H_{ik}|^2 S_{\hat{w}_k} d\nu, \quad i = 1, 2 \tag{5.7}$$

and with the white noise in equation 5.1, the disturbance spectra given in equation 5.3, and the coupled roll-pitch vehicle dynamics given in equation 3.4, the above mean square response expression, after a little algebra, takes the form

$$\mathcal{E}[\omega_1^2] = \int_{-\infty}^{\infty} \frac{1}{|\Delta(j\nu)|^2} \left(\left[(\frac{c_2}{I_1 I_2})^2 + (\frac{\nu}{I_1})^2 \right] S_{\tau_1} + (\frac{h_{_B}}{I_1 I_2})^2 S_{\tau_2} \right) d\nu \tag{5.8}$$

$$\mathcal{E}[\omega_2^2] = \int_{-\infty}^{\infty} \frac{1}{|\Delta(j\nu)|^2} \left((\frac{h_{_B}}{I_1 I_2})^2 S_{\tau_1} + \left[(\frac{c_1}{I_1 I_2})^2 + (\frac{\nu}{I_2})^2 \right] S_{\tau_2} \right) d\nu \tag{5.9}$$

The mean square response of the roll-pitch angular velocities can then be written as

$$\begin{aligned} \mathcal{E}[\omega^T \omega] &= \mathcal{E}[\omega_1^2] + \mathcal{E}[\omega_2^2] \\ &= \frac{1}{h_{_B}^2} \int_{-\infty}^{\infty} \frac{1}{p(j\nu)} \left(\left[1 + (\frac{c_2}{h_{_B}})^2 + \frac{I_2}{I_1} (\frac{\nu}{\lambda_o})^2 \right] S_{\tau_1} \right. \\ &+ \left. \left[1 + (\frac{c_1}{h_{_B}})^2 + \frac{I_1}{I_2} (\frac{\nu}{\lambda_o})^2 \right] S_{\tau_2} \right) d\nu \end{aligned} \tag{5.10}$$

where

$$p(j\nu) \triangleq \left[(\frac{\alpha}{\lambda_o})^2 + (\frac{\nu}{\lambda_o} + \beta)^2 \right] \left[(\frac{\alpha}{\lambda_o})^2 + (\frac{\nu}{\lambda_o} - \beta)^2 \right] \tag{5.11}$$

and

$$\alpha \triangleq \frac{1}{2} \left(\frac{c_1}{I_1} + \frac{c_2}{I_2} \right), \qquad \beta \triangleq \sqrt{1 - \frac{1}{\lambda_o^2} \left(\alpha^2 - \frac{c_1 c_2}{I_1 I_2} \right)} \tag{5.12}$$

For sizing purposes, consider simple yet physically consistent approximations to the mean square formula given in equation 5.10. In addition to assumptions in equations 4.6 and 5.4, by limiting the disturbance bandwidth with respect to the precession frequency as given in equation 4.6, i.e.,

$$\frac{\nu}{\lambda_o} \ll 1 \tag{5.13}$$

terms with the frequency ratio, $\frac{\nu}{\lambda_o}$, appearing in the integrand in equation 5.10 can be ignored. In summary, if one approximates the integrand in equation 5.10 by its value at $\nu = 0$, i.e., its frequency response at low frequencies, one can readily obtain

$$\mathcal{E}[\omega^T\omega] \approx \frac{1}{h_B^2\left[1+\frac{c_1c_2}{h_B^2}\right]^2}\left(\left[1+(\frac{c_2}{h_B})^2\right]\mathcal{E}[\tau_1^2]+\left[1+(\frac{c_1}{h_B})^2\right]\mathcal{E}[\tau_2^2]\right) \tag{5.14}$$

$$= \frac{1}{h_B^2\left[1+(\frac{c}{h_B})^2\right]}\mathcal{E}[\tau^T\tau] \qquad \text{if } c_1 = c_2 = c \tag{5.15}$$

$$\approx \frac{1}{h_B^2}\mathcal{E}[\tau^T\tau] \qquad \text{if } c_1 = c_2 = c \text{ and small damping } \zeta \ll 1 \tag{5.16}$$

Notice that the approximation formulas in equations 5.14 to 5.16 can be obtained directly from the state equations in 3.1 without considering the integral given in equation 5.10. This is done by (1) neglecting inertial torques/angular acceleration terms to obtain the approximate formula in equation 5.14, (2) additionally assuming $c_1 = c_2 = c$ to obtain equation 5.15, and (3) additionally assume small damping to obtain equation 5.16. All the above approximations assume a low frequency response wherein inertial torque or angular acceleration effects are sufficiently small such that the angular velocity response is dominated by the gyroscopic "stiffness" effects and precession damping. Analogous to a spring-mass-dashpot system, notice that the the gyroscopic "stiffness" appear as conservative restoring torques, but they are proportional to cross angular velocities, ω_1, and ω_2, and the level of bias momentum is analogous to the degree of "stiffness". The approximate formulae in equations 5.14 to 5.16 do not depend on the inertia of the vehicle, I_1, and I_2, because the inertial effects are assumed small at low frequencies. Only the gyroscopic "stiffness" term, h_B, approximately defines the angular velocity response to torque at low frequencies.

5.3 Explicit Integration Approximation

The following sections derive and examine response formulae from explicit integrations for two classes of systems: (1) with no damping, and 2) viscously damped.

5.3.1 Undamped System

For the zero viscous damping case, the MSR of the angular velocities from equation 5.10 is written as

$$\varepsilon[\omega^T\omega] = \frac{1}{h_B^2}\int_\infty^\infty \frac{1}{p(j\nu)}\left(S_{\tau_1}+S_{\tau_2}+[\frac{I_2}{I_1}S_{\tau_1}+\frac{I_1}{I_2}S_{\tau_2}](\frac{\nu}{\lambda_o})^2\right)d\nu, \quad x_o < 1 \tag{5.17}$$

where

$$x_o \triangleq \frac{BW_\tau}{\lambda_o} \tag{5.18}$$

Under the assumption that the PSD of the anticipated disturbance torque is approximated by constants, $S^o_{\tau_1}$ and $S^o_{\tau_2}$ (see discussions surrounding equation 4.6), the integral of equation 5.17 is solved using indefinite integrals as described in the Appendix and is written as

$$\varepsilon[\omega^T\omega] = \frac{\lambda_o}{h_B^2}\left((k_1+k_2)\frac{x_o}{1-x_o^2} + 0.5(k_1-k_2)\ln(\frac{1+x_o}{1-x_o})\right), \quad x_o < 1 \tag{5.19}$$

where

$$k_1 \triangleq S^o_{\tau_1} + S^o_{\tau_2}, \quad k_2 \triangleq \frac{I_2}{I_1}S^o_{\tau_1} + \frac{I_1}{I_2}S^o_{\tau_2} \tag{5.20}$$

Consistent with physical expectations where an undamped mode excited harmonically will result in an instability, the condition $x_o = 1$ in equation 5.19 predicts an infinite response in MSR. Clearly, for an undamped system, the disturbance bandwidth cannot equal or exceed the precession frequency so that the undamped response integral, equation 5.17, and its approximate solution, equation 5.19, are valid only for $BW_\tau < \lambda_o$.

Special Case $I_1 = I_2 = I$ **:** In this case, equation 5.19 with the aid of equation 5.4 reduces to

$$\varepsilon[\omega^T\omega] \approx \frac{1}{h_B^2(1-x_o^2)}\varepsilon[\tau^T\tau] \tag{5.21}$$

5.3.2 System with Damping

For the non-zero viscous damping case, the integral expression in equation 5.10 is solved explicitly using indefinite integrals outlined in Appendix and is written as

$$\begin{aligned}\varepsilon[\omega^T\omega] \;=\; & \frac{\lambda_o}{h_B^2}\left\{\frac{1}{4\beta}\left(\frac{k_3}{\zeta_m^2+\beta^2}-k_2\right)\ln\left(\frac{(x_o+\beta)^2+\zeta_m^2}{(x_o-\beta)^2+\zeta_m^2}\right)\right. \\ & \left. +\frac{1}{2\zeta_m}\left(\frac{k_3}{\zeta_m^2\beta+\beta^2}+k_2\right)\left[\tan^{-1}\left(\frac{x_o-\beta}{\zeta_m}\right)+\tan^{-1}\left(\frac{x_o+\beta}{\zeta_m}\right)\right]\right\}\end{aligned} \tag{5.22}$$

where β, ζ_m, and k_2 are defined in equations 5.12, 3.6, and 5.20 respectively and

$$k_3 \triangleq [1+(c_2/h_B)^2]S^o_{\tau_1} + [1+(c_1/h_B)^2]S^o_{\tau_2} \tag{5.23}$$

Since the explicit formula in equation 5.22 is nice but difficult to visualize, consider the following simplifying assumptions: $I_1 = I_2 = I$ and $c_1 = c_2 = c$ in order to gain more physical insight. In section 6.1.1, estimates of these errors are computed by numerical simulation and it appears that even if these assumptions are not exactly satisfied, these approximations appear to be sufficiently accurate for design and sizing purposes. With these assumptions the following parameters simplify to

$$k_3 = [1+(c/h_B)^2]k_2, \quad \zeta_m = c/h_B, \quad \beta = 1 \tag{5.24}$$

so that after substituting for the mean square torque in equation 5.4, equation 5.22 reduces as follows:

$$\varepsilon[\omega^T\omega] \approx \frac{\varepsilon[\tau^T\tau]}{2cI(BW)_\tau}\left[\tan^{-1}\left(\frac{x_o-1}{\zeta_m}\right)+\tan^{-1}\left(\frac{x_o+1}{\zeta_m}\right)\right] \tag{5.25}$$

Special Case $\zeta_m \ll 1$, $x_o < 1$ **:** This case applies for small damping and where the disturbance bandwidth is less than its precession frequency. For this case, the response in equation 5.25 simplifies to

$$\varepsilon[\omega^T \omega] \approx \frac{1}{h_B^2(1-x_o^2)} \varepsilon[\tau^T \tau] \tag{5.26}$$

The formula predicts that MSR varies with the inverse square of the bias momentum level. As the disturbance bandwidth approaches the lightly damped precession frequency from below, the MSR is predicted to increase by the inverse factor of $(1-x_o^2)$. With small disturbance bandwidth and large precession frequency or bias momentum, the above formula for MSR matches both the static approximation derived previously in equation 5.16, and the undamped special case based on explicit integration approximation given in equation 5.21.

Special Case $\zeta_m \ll 1$, $x_o > 1$ **:** This case applies also for small damping but where the disturbance bandwidth is greater than its precession frequency. For this case, equation 5.25 simpifies to

$$\varepsilon[\omega^T \omega] \approx \frac{\pi}{2cI(BW)_\tau} \varepsilon[\tau^T \tau] \tag{5.27}$$

When disturbance bandwidth is larger than precession frequency, the formula predicts that the MSR of the angular velocities will not be dependent on bias angular momentum. This is because with small damping, the MSR will be dominated by the large response in the lightly damped precession mode. As long as the disturbance bandwidth equals or exceeds the precession frequency, the contributions to MSR from higher frequencies will be small. The formula also predicts that larger inertia platform and damping levels will result in smaller MSR to disturbances. Finally, the MSR is also inversely proportional to disturbance bandwidth which reflects the fact that for a given mean square disturbance torque, its spectral density, inversely proportional to its bandwidth, will be spread out well beyond the bandwidth of the system, so that the system response will be less with increasing bandwidth of the disturbance.

Special Case $\zeta_m \gg 1$, **any** x_o **:** This case applies for large damping for any disturbance bandwidth. Using the Taylor expansion of $\tan^{-1}$ written in Appendix, equation 5.25 can be approximated as

$$\varepsilon[\omega^T \omega] \approx \frac{\varepsilon[\tau^T \tau]}{c^2} \tag{5.28}$$

With large damping, equation 5.28 predicts that the MSR of the angular velocity will be dependent only on the damping coefficient. Physically, this is the case where the damping torques in the system dominates over both gyroscopic and inertia torques. The analogy to a spring-mass-dashpot system is a response to disturbances when both the mass and stiffness in the system are very small, a very unlikely scenario in the scope of applications of interest in this study.

6 Bias Momentum Sizing

In general, the sizing of bias momentum to improve directional stability depends on many factors and parameters including vehicle inertial parameters, anticipated disturbance environment, and the degree of response attenuation desired by gyric stiffning. An important end goal in designing an effective level of bias momentum is to mitigate the vehicle attitude response to unknown external disturbances. If the attitude response is measured in terms of mean-square response of the roll and pitch angular velocities in response to a specific bandlimited external disturbance torques, the approximate analytical formula given in equation 5.25 can be useful in terms of both sizing and qualitatively understanding the key factors and parameters. However, in any given physical application, it is the role of the design engineer to choose a physically suitable metric to quantify the vehicle attitude response and to secure a physically relevant model of the anticipated disturbance environment.

Consider the following approximate but analytical MSR derived earlier in equation 5.25. Using the above expression, various special cases can be derived, including those given by equations 5.16, 5.21, 5.26, 5.27, and 5.28. In a typical sizing problem, one would expect to be given, at miniumum, the vehicle inertia, the disturbance bandwidth, and some idea of the level of damping in the system (c is either zero, "small" or "large"). With this basic information, the question is what level of bias momentum would be helpful in terms of mitigating the roll-pitch MSR to this assumed form of disturbances.

To numerically examine the above sizing equations, consider the flying dual-spin system called the Dual Spin Test Device (DSTD) as shown in Figure 4. The DSTD is an indoor

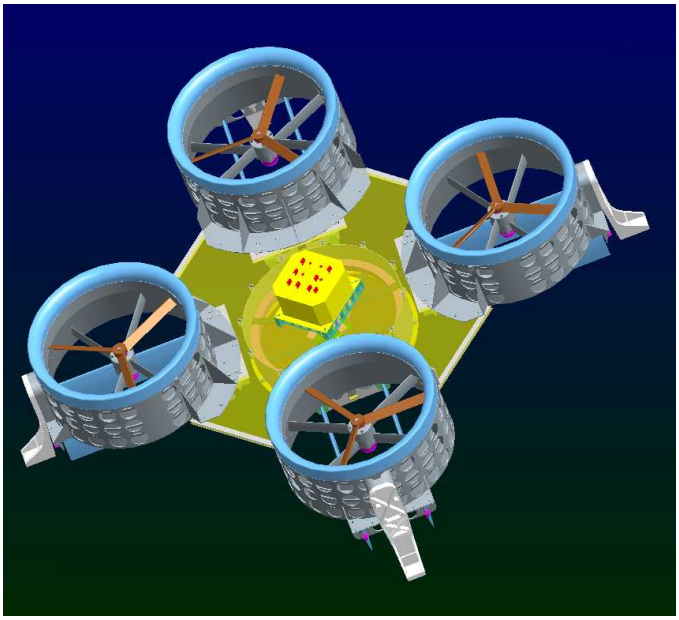

Figure 4: DSTD: A generic dual spin test device.

flying platform at NASA Langley Research Center designed to validate dynamics and stability characteristics of a generic VTOL platform. It consists of a square honeycomb main body

with four ducted propellers fixed to the corners of the main body. A pair of control vanes are attached to the aft of each duct and a momentum wheel is attached to the bottom of the main platform. For more details on the DSTD, see [19],[20],[21]. Table 1 shows the values for nominal parameters used for sizing a momentum wheel.

Parameter	*Symbol*	*Value*
vehicle mass	m	16.8 kg
vehicle length,width, height	l_1, l_2, l_3	0.9, 0.9, 0.3 m
vehicle roll, pitch, & yaw inertias	I_1, I_2, I_3	0.59, 0.58, 1.15 $kg - m^2$
design disturbance torque variance	$\epsilon[\tau^T\tau]$	14 N^2m^2
design disturbance torque bandwidth	$(BW)_\tau$	3.2 Hz
system damping	ζ	small but unknown

Table 1: Nominal parameters values for DSTD.

6.1 Dependence on System Damping

Figure 5 shows the dependence of MSR on the levels of bias momentum and damping levels based on equation 5.25. Specifically, viscous damping coefficients of $c = [0.01,\ 0.1,\ 1,\ 10,\ 100]$ are shown. The general trend is that the MSR decreases with increasing h_B and damping

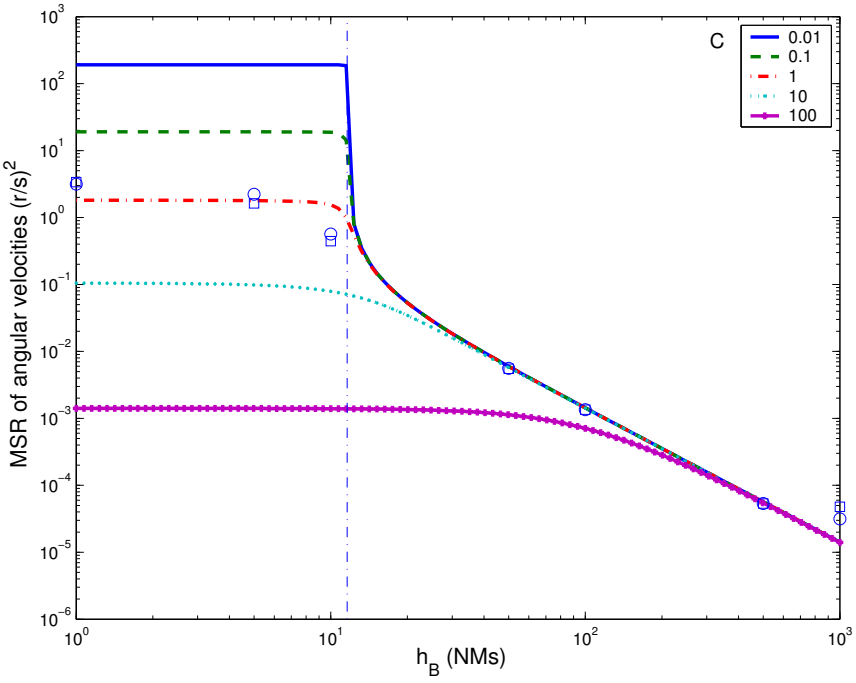

Figure 5: MSR dependence on bias momentum for different levels of damping.

in the system. Notice that based on the level of bias momentum, there appears to be three

different trends in the response. In Figure 5, the dashed-dotted vertical line indicates the angular momentum level such that

$$h_{_B} = (BW)_\tau I \quad \Leftrightarrow \quad x_o = 1$$

At this angular momentum level, the precession frequency λ_o is the same as the disturbance bandwidth $(BW)_\tau$. This level can be viewed as a boundary between the "low" and the "intermediate/high" levels of bias momentum.

For "low" bias momentum levels (on the left of the dash-dotted line), given a level of damping, the MSR is insensitive to different levels of bias momentum. In this case where $x_o \geq 1$, the disturbance bandwidth is greater or equal to the precession frequency so that for small damping, the vehicle response will be dominated by a lightly damped precession mode. Once the lightly damped precession mode is excited and dominates the response, increasing the disturbance bandwidth or decreasing the bias momentum level will not change the MSR significantly. The special case responses given in equation 5.27 for small damping and equation 5.28 for large damping corresponds to this case.

At intermediate or high momentum levels (on the right of the dash-dotted line) where $x_o < 1$, the disturbance bandwidth is less than the precession frequency so that as x_o decreases, the precession mode will be excited even less, with a factor of $1/(1 - x_o^2)$, as seen in equations 5.21 and 5.26. Hence, at an intermediate $h_{_B}$ level, where $x_o \approx 1$, the MSR is very sensitive (apparent even in log-log scale) to the level of bias momentum. Finally, at a high level of $h_{_B}$, the MSR decreases at two orders of magnitude per an order of magnitude increase in $h_{_B}$ level.

6.1.1 Validation of Approximate Analytical Formula

To validate the approximations given in equation 5.25, these predictions are compared with detail simulation results from a fully nonlinear dynamical system response of the generic flying dual-spin system as described earlier. Based on a simulated sample disturbance torque of bandwidth 20 r/s and a damping level of $c = 1$, simulated responses at bias momentum levels of $[1, 5, 10, 50, 500]$ Nms in the system are computed and represented by circles ($\circ$) in Figure 5. Notice that the MSR based on the full non-linear simulation is close to the predicted MSR (represented by the dash-dot line), which validates the response approximation formula as given in equation 5.25.

Figure 6 shows the angular velocity time responses in the roll axis for different levels of bias momentum in the vehicle system. Notice the different scales used to show the responses. It is clear that higher bias momentum levels can significantly attenuate angular velocity response of the vehicle.

To simulate the errors incurred by violating the assumption of equal rotational inertias in the roll and pitch axes, the full nonlinear dynamics with $I_2/I_1 = 0.7$ is considered, and the results are shown in Figure 5 as square ($\square$) symbols. Again, the simulation results, with the additional error due to unequal vehicle inertias, indicate a good match between the predicted response and the detailed simulation MSRs.

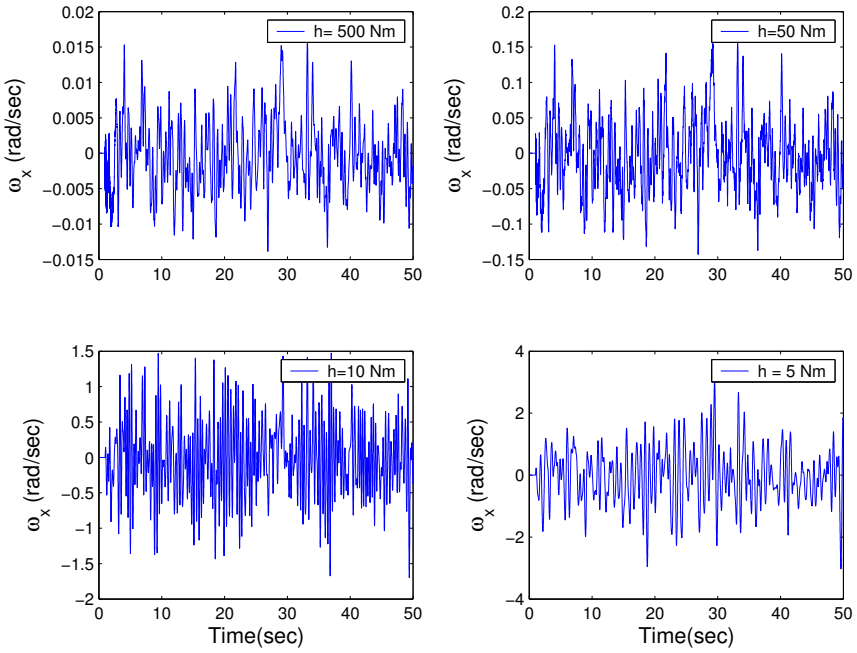

Figure 6: Roll angular velocity responses to disturbances at bias momentum levels of $[5, 10, 50, 500]$ Nms and damping level of $c = 1.0$.

Finally, notice from Figure 5 that the high degree of match in the MSR, especially at the higher bias momentum levels (or more specifically $x_o \ll 1$), is due to the condition of bias momentum dominance as discussed earlier in equation 2.13. When the bias momentum level is *gyroscopically dominant*, the roll and pitch dynamical response becomes essentially linear, even at large angular velocities.

6.2 Dependence on Vehicle Inertia

Figure 7 shows the dependence of MSR on bias momentum levels for the following levels of vehicle inertia, $[1,\ 2,\ 5,\ 10,\ 50]I$ where $I = 0.58\ kg - m^2$. The damping coefficient of $c = 1.0$ is assumed for all cases. As is clear from Figure 7, in general, the MSR value decreases with increasing bias momentum, and at higher bias momentum levels, the gyroscopic effects dominate and produces a second order decrease in MSR with increasing bias momentum.

The dependence of MSR on the level of vehicle inertia, for a fixed level of bias momentum is slightly more complicated. At lower bias momentum levels, say $h_{_B} = 5\ Nms$, the MSR decreases with increasing levels of vehicle inertia. However, at higher bias momentum, for example at $h_{_B} = 20\ Nms$, it is evident from Figure 7 that the MSR for a vehicle with inertia I is predicted to have a much smaller MSR than corresponding vehicles with larger inertias of $2I$, $5I$, and $10I$. This counter-intuitive trend, that smaller inertia vehicles can give smaller responses than larger inertia vehicles for a fixed level of disturbances and bias momentum, follows from the fact that for a given level of bias momentum, smaller inertia vehicles more readily exhibit gyroscopic effects, as captured by the key parameter value of, $x_o < 1$. In other

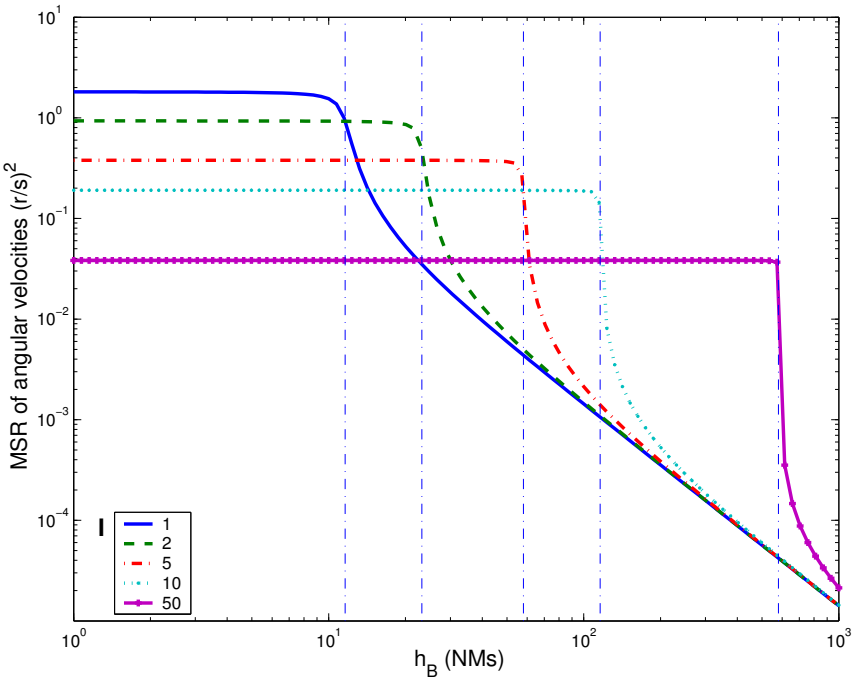

Figure 7: MSR dependence on bias momentum for different levels of vehicle inertia, at $c = 1.0$.

words, the attenuation due to gyroscopic effects is greater than that due to reduction of motion due to an increase in inertia. For the extreme case with the very large inertia of $50I$, the MSR finally becomes slightly lower than that for a vehicle with inertia I, at $h_{_B} = 20\ Nms$.

Notice that at $h_{_B} = 20\ Nms$, only the smallest inertia vehicle with inertia I is expected to exhibit gyroscopic effects with a precession frequency of $\lambda_o = h_{_B}/I = 34.5$ r/s, which is significantly higher than the disturbance bandwidth, $(BW)_\tau = 20$ r/s, and equivalently $x_o = 0.58 < 1$. All the larger inertia vehicles, for example, a vehicle with inertia $10I$ will have a much lower precession frequency of $\lambda_o = h_{_B}/I = 3.4$ r/s so that $x_o = 5.9 > 1$, will not exhibit significant attenuation due to gyroscopic effects.

The dashed-dotted vertical line in Figure 7 indicates the angular momentum level such that (for a given vehicle inertia) the precession frequency λ_o is the same as the disturbance bandwidth $(BW)_\tau$. This critical line increases with increasing vehicle inertia. This means that for larger inertia vehicles, higher levels of bias momentum are needed to induce sufficient gyric stability.

6.3 Design Summary for DSTD

Figure 8 shows a summary of relevant DSTD characteristics in the selection of the bias momentum level for disturbance rejection, based on Figure 5. A design range for the level of angular momentum needed is shown in Figure 8 along with the selected DSTD design of 17 Nms corresponding to $x_o = 0.69$ for a design disturbance as specified in Table 1. Its predicted response in terms of the standard deviation of the roll and pitch angular velocities is approximately

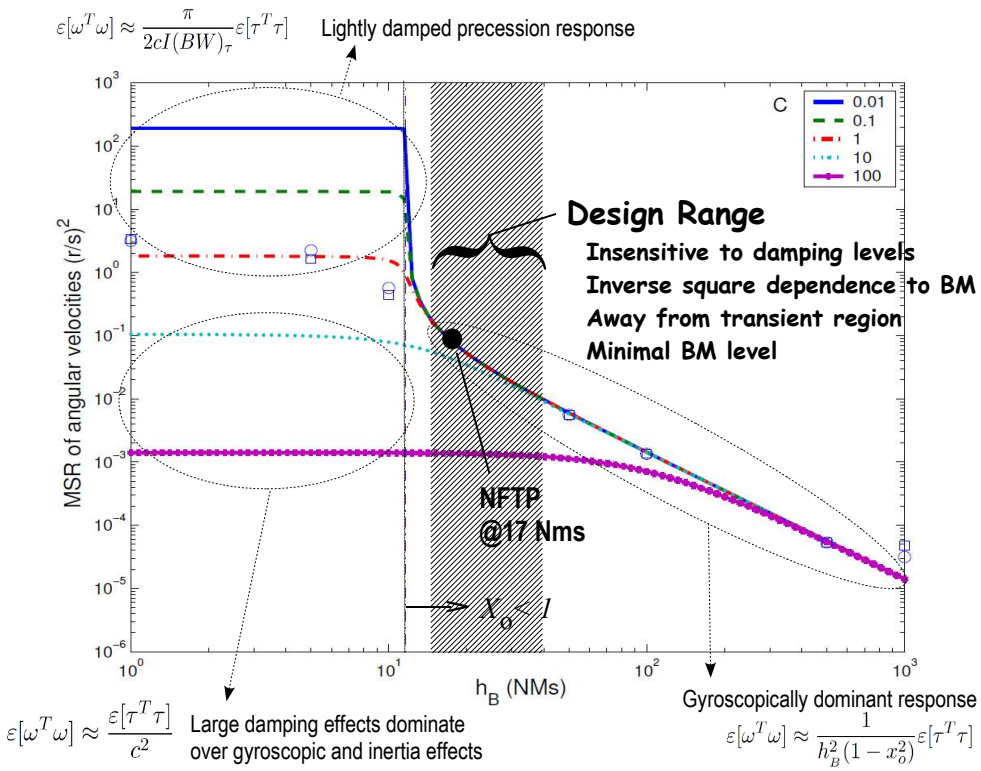

Figure 8: Summary of bias momentum sizing for DSTD.

17.4 deg/s. Of course the design response can be reduced further as necessary by implementing higher levels of angular momentum, for example, if the designed angular momentum is doubled to $h_{_B} = 34\ Nms$, the predicted response drops to 6.7 deg/s. Notice also that the predicted response is directly proportional to the standard deviation of the torque disturbance levels and the design disturbance level of $3.74Nm$ may be overly conservative.

The salient features of the design range indicated in Figure 8:

- The design range of $h_{_B}$ lies in the region where the designed Precesssion frequency, λ_o is greater than the designed disturbance bandwidth, $(BW)_\tau$, i.e., $x_o < 1$.
- The lower end of the design range is slightly greater than $h_{_B} = I \cdot (BW)_\tau = 10.9\ Nms$, to avoid the large transient increase in response by the factor $(1 - x_o^2)$. The high end of the design range is driven by the need to limit the bias momentum level required, to mitigate weight and size requirements.
- The design range lies in a region where the gyroscopic effects dominante the response and the response MSR has an inverse square dependence on the level of angular momentum.
- In the design response range, the MSR is insensitive to damping levels in the system, with the exception that large damping effects dominate over gyroscopic and inertia torques, a physically unlikely scenario. This is an important advantage because damping levels for systems are typically difficult to model and predict accurately.

A physical realization of a bias momentum wheel designed for 17 Nms is shown in Figure 9 and

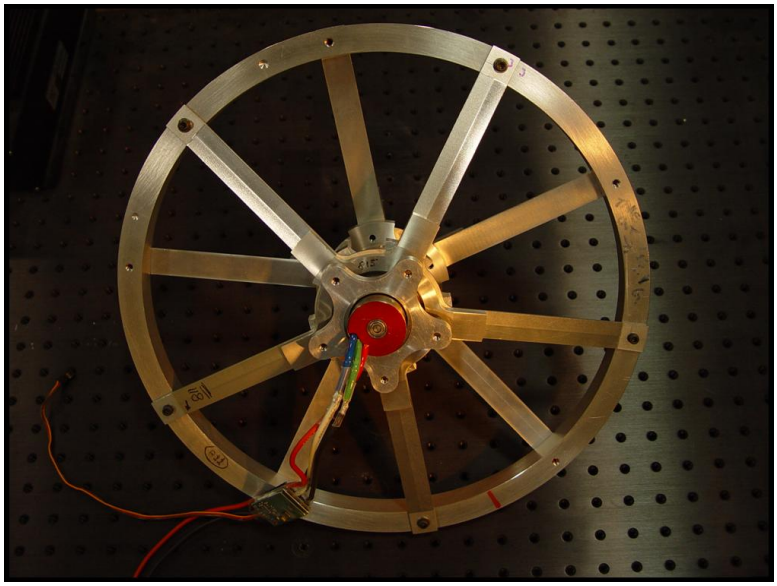

Figure 9: A momentum wheel fabricated for DSTD.

consists of a flywheel having a diameter of 0.39 m, ring mass of 1.08 kg (6.4 % of gross weight of DSTD vehicle), and spinning nominally at 4000 rpm. As much as technologically feasible, the mass of the flywheel can be reduced by either increasing the diameter of the flywheel or the flywheel spin rate.

In sizing bias momentum for the purpose of mitigating a vehicle response to external disturbances, the simplest approach is to either increase damping sufficiently (Figure 5), and/or increase inertia sufficiently (Figure 7) such as to satisfy a certain desired level of MSR for the particular vehicle. In both approaches, dual-spin stabilization using bias momentum is not necessary. However, increasing vehicle damping or inertia sufficiently for a free-flying vehicle may be detrimental to performance or even be physically unrealizable, for a VTOL application.

The alternative to the above predicament is to "roll-off" the MSR with sufficiently large bias momentum, i.e., dual-spin stabilize the vehicle. A generally desirable goal then is to select a bias momentum level which is on the $1/h_B^2$ slope, i.e., for a given vehicle inertia and disturbance bandwidth, choose a bias momentum level such that the precession mode frequency will exceed the disturbance bandwidth to some chosen margin, or based on equation 3.8,

$$h_B > (1 + \text{margin})\sqrt{I_1 I_2}(BW)_\tau \tag{6.1}$$

Of course, avoiding exciting the precession frequency will be particularly important if the precession motion is undamped or only very lightly damped. By going further to the right side of the vertical line (where $x_o = 1$), the MSR becomes less and less dependent on inertia and damping changes. In the extreme case where $x_o \ll 1$, the above simplifying behavior approaches static approximations, meaning that the disturbance bandwidth is well below the precession frequency. In general, one could size the bias momentum based on a requirement to stay below a target mean square response as given in equation 5.25 or below a target frequency response as given in equation 4.14.

7 Simulation Results

This subsection show various results based on DSTD vehicle simulation that demonstrates the advantages in using bias momentum in a flying platform. The significant improvements in the vehicle attitude control robustness to disturbances are not limited to open loop hovering conditions. The simulation results indicate that improvements in performance can extend to closed loop response, command tracking, and even payload changes during flight. Interestingly, simulation results also demonstrates that the use of bias momentum is most dramatic under larger disturbances in payload or winds.

This subsection describes simulation results based on full nonlinear models that are constructed from first principles, bench test data refined model parameters, sampled and quantized measurements, and saturation limits on actuators. In particular, the dynamical models for the ducted propeller/vane, whose development are based on bench tests, includes asymmetrical effects which are difficult to visualize due to their 3-dimensional characteristics. This MATLAB-Simulink simulation model also incorporates models of servo dynamics that regulate fan speeds and vane angles.

In the simulation cases that follow, the vane angles and the fan speeds are actively used for stabilization and control which reflects the current state-of-the art approach based on vector and differential thrusting. Initially, the simulation focused on the effects of bias momentum in the stabilization and control performance of the flying test platform. Gyroscopic stability effects are highlighted by comparing a system with significant level of bias momentum (BM cases) with a corresponding system with no bias momentum (NBM). A difference in this study is the independent control of all four propeller speeds and their respective vane angles, as opposed to constraining it to work in pairs and collectively, as in conventional helicopter control [22],[23] or practically all VTOL flying platforms [24].

7.1 Crosswind and turbulence model

To simulate wind disturbances during hovering or low airspeed operations, crosswinds are assumed to be impinging on a vertical cylinder attached to the upper part of the platform, as shown in Figure 10. The resulting aerodynamic forces on this cylindrical column is used to simulate the crosswind and turbulence on the vehicle. The empirical model given in [25] for aerodynamic forces over a cylindrical column is used. The resulting disturbance model consists of forces and torques in the pitch and roll axes. Two sets of winds are simulated, namely, "light" winds, and "strong" winds. The "light" winds simulate "calm to gentle breeze" with sample mean wind speeds of 7 Knots and standard deviation of 5. However for "strong" winds, intended to simulate "calm to strong breeze/near gale", the simulated sample mean wind speed is 15 Knots with a standard deviation of 18, as seen in Figure 11.

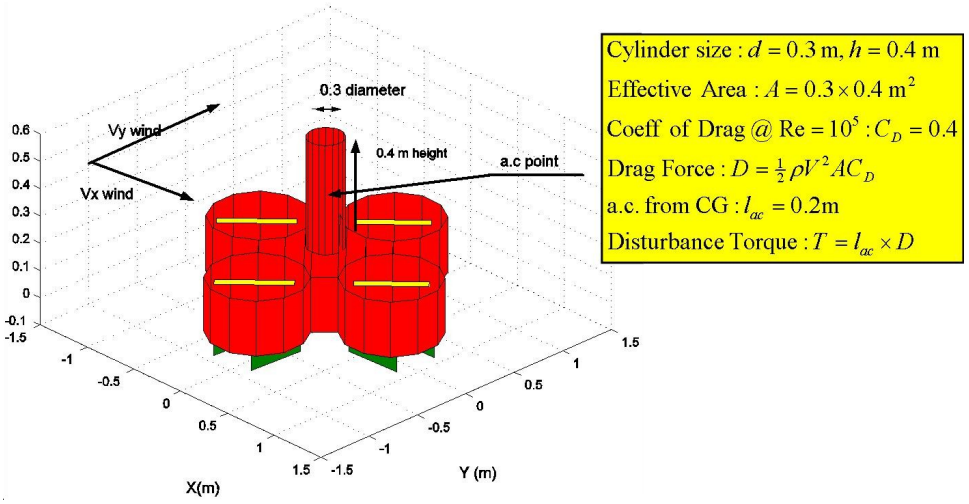

Figure 10: Simulated turbulent crosswinds on DSTD.

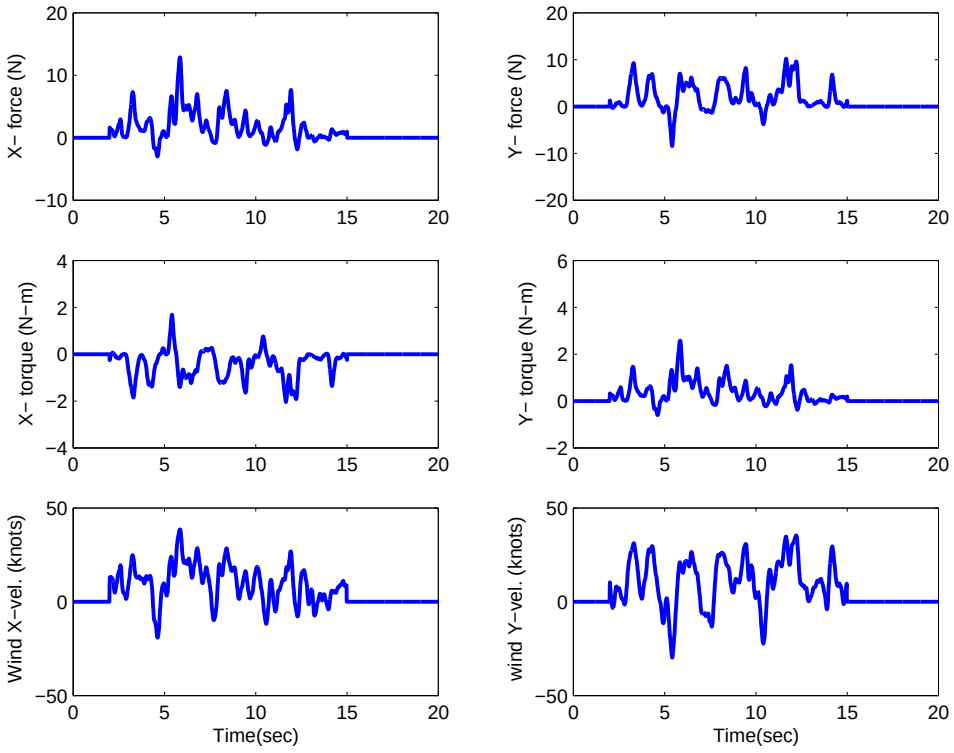

Figure 11: Simulated strong wind.

7.2 Controller Law Synthesis

Figure 12 shows a schematic of the model used for control law design and simulation. The

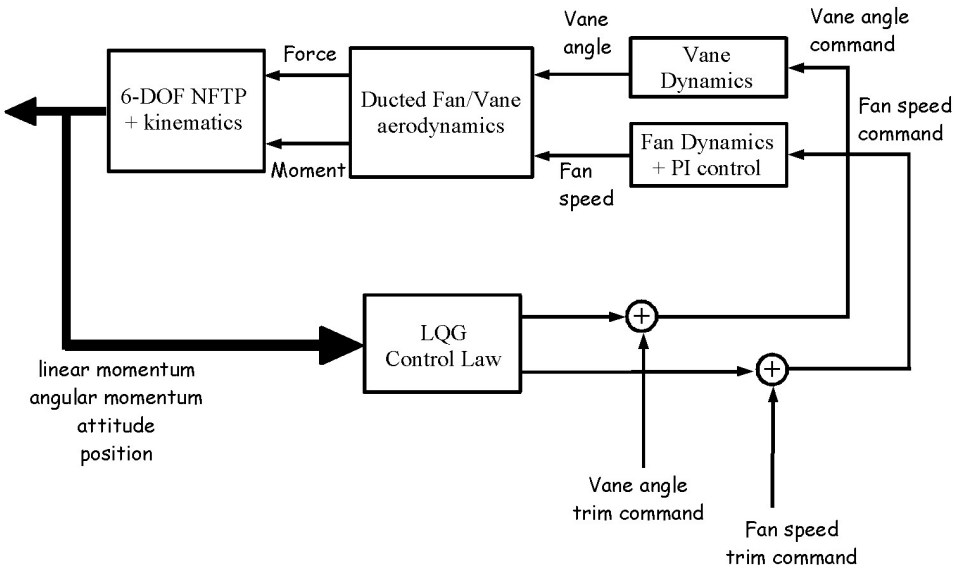

Figure 12: DSTD model used for control law design and simulation.

DSTD mathematical model with fan and servo models has 24 states consisting of 3 linear momenta, 3 angular momenta, 3 attitudes, 3 positions, 8 fan motor states, and 4 vane servo motor states. The 8 fan motor states include for each ducted fan, first order PI controllers to regulate individual fan speeds which are assumed governed by first order dynamics. Based on LQG control theory (see for example [16]), feedback controllers are designed to stabilize and hold the platform attitude and also track the translational velocity and angular velocity commands. In all cases, 4 vane angles and 4 fan speeds were commanded. For control during both hovering and velocity tracking, 12 states including 3 attitudes, 3 angular velocities, 3 positions, and 3 linear velocities were used for feedback by the LQG controller. In this simulated design study, feedback controllers for the BM and NBM cases are synthesized based on the linearized model about hovering trim, which is identical to the trim conditions at a constant translational velocity if aerodynamics due to vehicle airspeed are not included, as assumed in this study due to their low dynamic pressures. For a fair comparison between BM and NBM cases, the same LQG weights were used in the controller design

A key difference in the BM and NBM cases is that in the BM case, each pair of fans are counter rotated to mitigate both inertial and aero-resistance fan drag torques due to fan rotations, as compared to same-direction rotation of all four fans in the BM case. Consequently, the trim conditions in BM and NBM cases are necessarily different since the net aero-resistance fan drag torques are different, and must be statically canceled by vane-deflected forces.

Figure 13 shows the tradeoff between performance cost and control effort for a parameterized set of LQG controllers undergoing gust response during hover over a period of time T_{final}. The quadratic cost function used in the LQG control law included six states for position and velocity

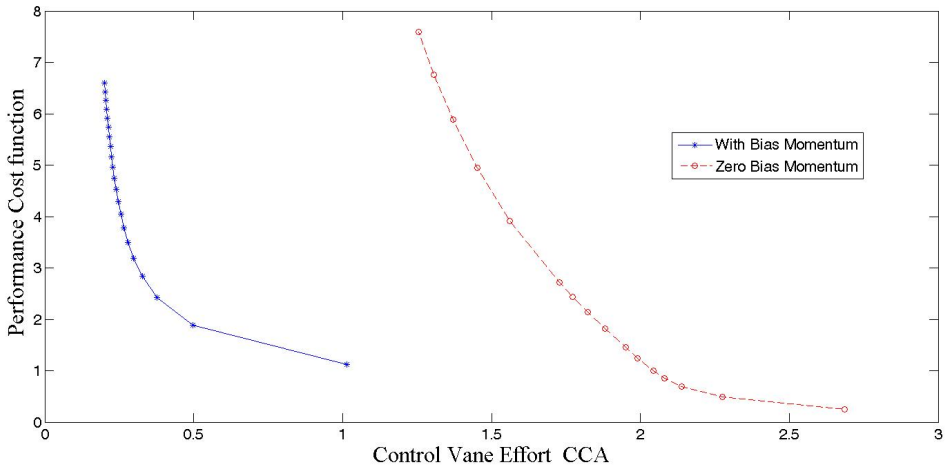

Figure 13: Control effort (abscissa) vs Performance cost (ordinate) for a parameterized set of LQG controllers undergoing gust response during hover.

and six states for attitude and angular rates. The different controllers were parameterized by scaling the quadratic control penalty term consisting of four vane angles and four fan speeds excursions about their individual trim values. For ease of comparison of closed loop performance among different LQG control laws and for both cases with BM and NBM, consider only a subset of variables. Specifically, the performance cost in terms of attitude (β_i) and position (ξ_i) errors are

$$J(t) \triangleq \int_0^t \sum_{i=1}^{3} [(\beta_i - \hat{\beta}_i)^2 + (\xi_i - \hat{\xi}_i)^2] dt \tag{7.1}$$

and the control effort is defined by a cumulative control activity (CCA) function as follows

$$CCA(t) \triangleq \int_0^t \sum_{i=1}^{4} \dot{\theta}_i^2 dt \tag{7.2}$$

The above measure of control effort is a time integral of the sum of squares of all four control vane angular rates ($\dot{\theta}_i$). The abscissa and ordinate in Figure 13 represents $CCA(T_{final})$ and $J(T_{final})$ respectively. In addition to quantifying the level of control activity, the above control effort is intended to capture the level of control vane activity, which is seen as the primary source of control surface induced unsteady aerodynamics due to its thrust vectoring role. Albeit limited, this tradeoff study indicates that controllers are significantly more effective for a system endowed with significant levels of bias momentum (asterisk line) in terms of actuator effort necessary for a given level of performance cost. Although it is clear from this trade study that the NBM case requires significantly higher levels of vane control activity, the effect of controller induced unsteady aerodynamics is not included due to a lack of reliable model. However, one would expect to see a larger degradation of performance for the NBM cases.

7.3 Hovering

7.3.1 Open Loop Response to Light Winds.

The open-loop attitude responses of the initially trimmed system for the two cases are shown in Figure 14. In the NBM case (red line), the vehicle rapidly loses orientation and goes unstable, but in the BM case (blue line), the vehicle holds attitude inspite of a small gyric roll and pitch angle response to the light winds. However, the platform drifts off slowly without feedback compensation due to a steady wind component in the light winds.

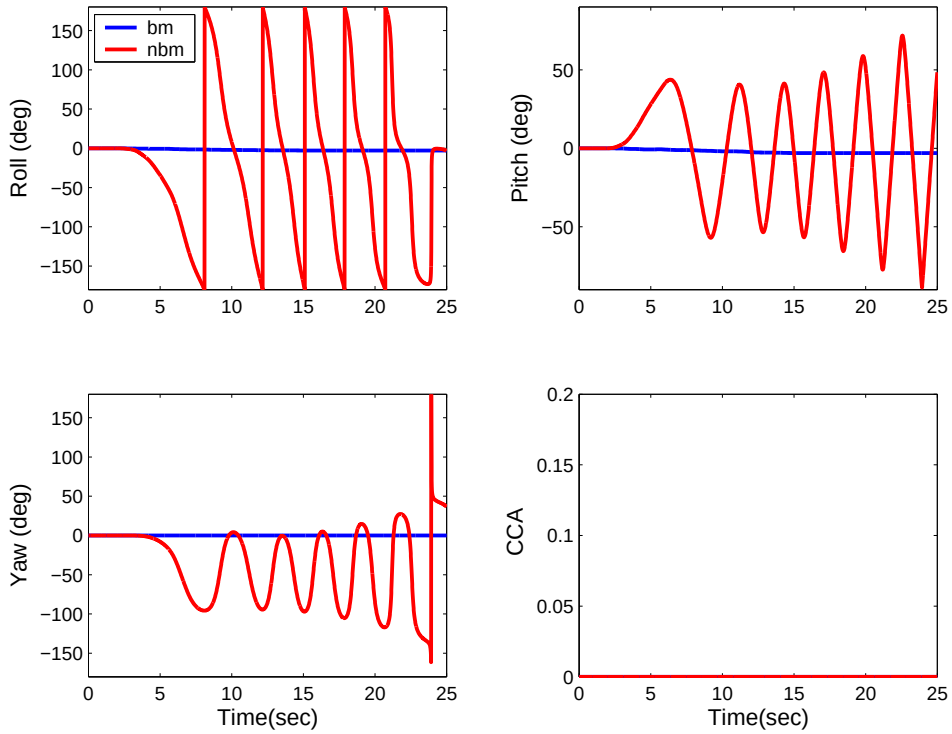

Figure 14: Open loop response to light winds, 3-2-1 Euler angles. BM Case (blue line), NBM Case (red line).

7.3.2 Closed Loop Response to Light Winds.

The closed-loop responses to light winds during hover for both cases are shown in Figure 15. Although both cases show stable response, the angular response for the BM case (blue line) is clearly less oscillatory and therefore superior to the NBM case (red line). Apparently, under these simulated light wind conditions, the angular response amplitudes for the NBM case appears to be small enough to be tolerated during an actual flight. The time history of the cumulative control effort (bottom right of Figure 15), shows that the case with BM actually requires less vane actuation than in the corresponding NBM case. As expected, the vane and fan actuator response did not saturate for both cases, under light winds.

7.3.3 Closed Loop Response to Strong Winds.

The closed-loop responses to strong winds during hover for both cases are shown in Figure 16. The controller for NBM case was judiciously scaled to mitigate actuator saturation. Both cases remains stable but the angular response for the BM case (blue line) is clearly less oscillatory and therefore superior to the NBM case (red line). However, the significantly larger angular response amplitudes for the NBM case will likely be unacceptable or even dangerous during an actual flight. The time history of the cumulative control effort shows that the case with BM requires less vane actuation and it gives far superior attitude hold than the corresponding NBM case.

To examine what happens if the controller for NBM case is not judiciously scaled to mitigate actuator saturation, resulting possibly to a more agressive feedback control, an additional simulation was done with the new control law. It turns out that the close loop system loses control after a few seconds. More specifically figures 17 and 18 shows the time histories of the vane angle and fan speed responses respectively. The vane and fan actuators saturate resulting in loss of vehicle under strong winds.

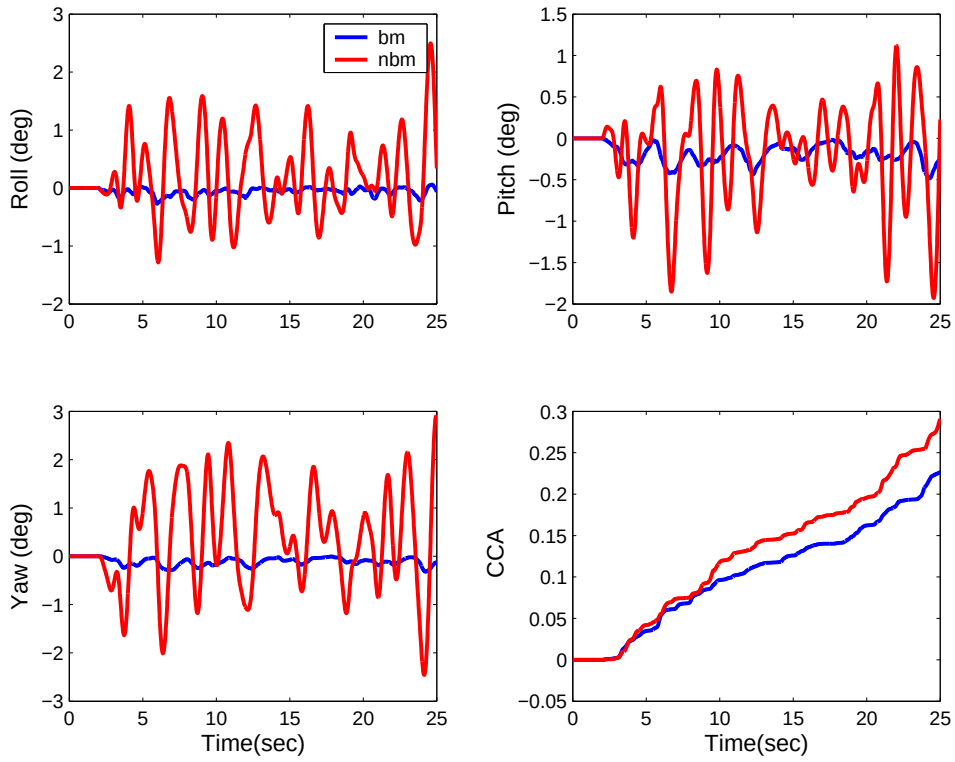

Figure 15: Closed loop response to light winds. BM Case (blue line), NBM Case (red line).

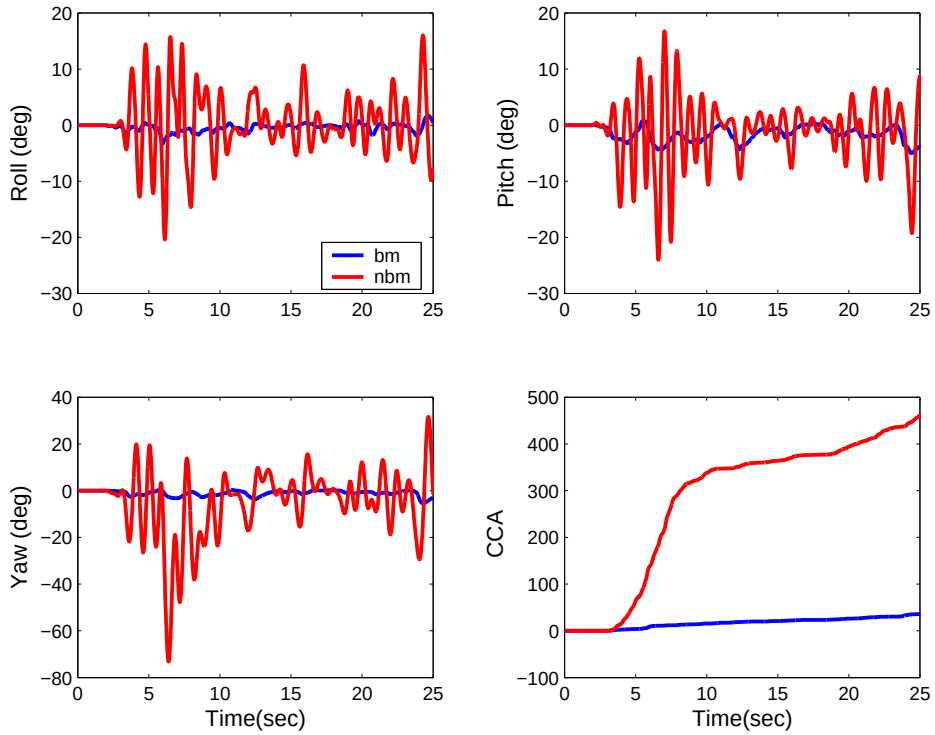

Figure 16: Closed loop response to strong winds. BM Case (blue line), NBM Case (red line).

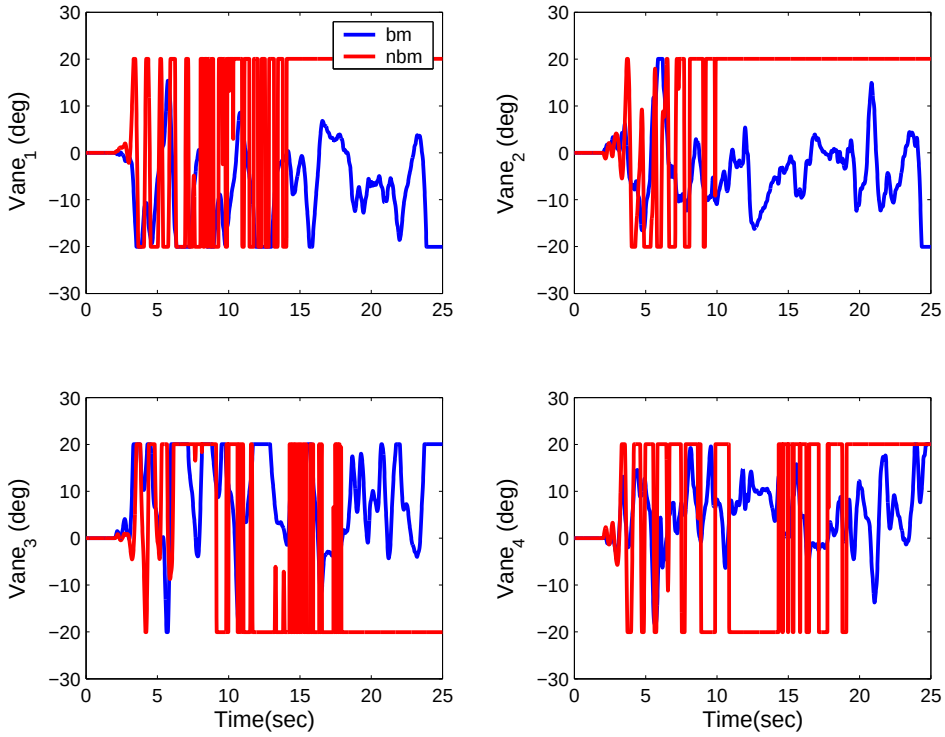

Figure 17: Closed loop response of control vanes to strong winds, more agressive control. BM Case (blue line), NBM Case (red line).

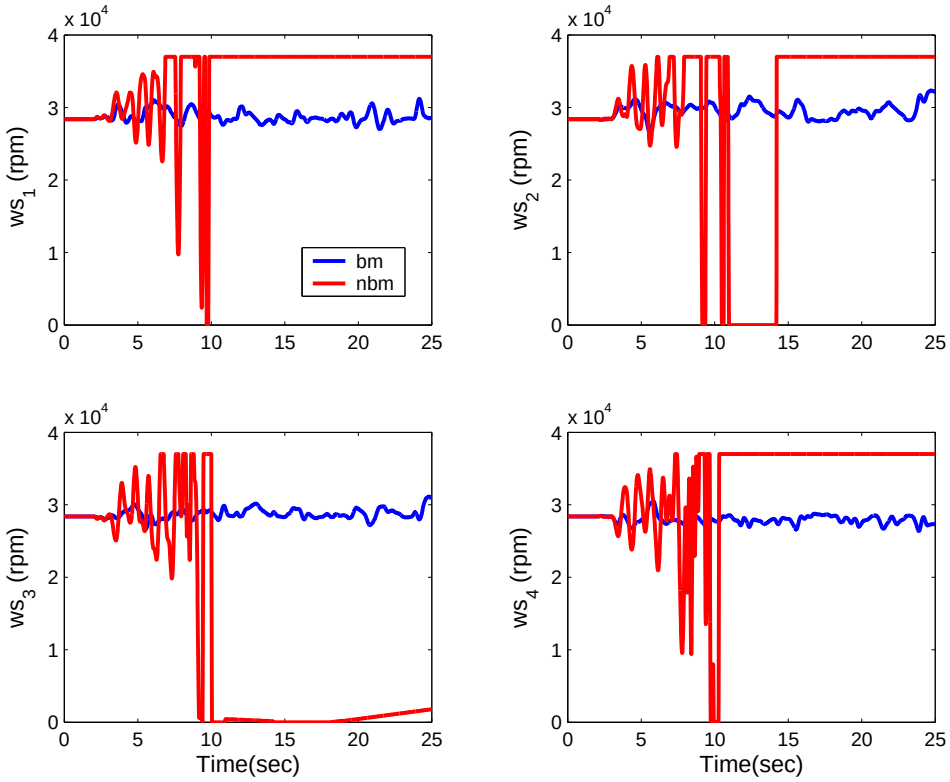

Figure 18: Closed loop response of fan speeds to strong winds, more agressive control. BM Case (blue line), NBM Case (red line).

7.4 Command Tracking

This section outlines a sample of simulation results of command tracking under strong winds, specifically translational velocity commands while holding a trim attitude. It should be noted that the demonstrated inherent advantage of bias momentum in endowing directional stability to the platform does not necessarily improve its maneuverability. Hence, the simulation results in this subsection is intended to examine this issue quantitatively.

For the following simulations, LQG based controllers are designed to track a trajectory path defined by a commanded translational velocities about trim with zero angular velocity. The input commands are shaped to mitigate the discontinuity in a step command. Figure 19 shows the response to translational velocity tracking commands (dashed green line) for both cases subject to strong winds. The accompanying excursions in the angular velocities (and hence the vehicle attitude) are shown in Figure 20. It is seen that for both cases, the vehicle can successfully track translational velocity commands but BM case (blue line) gives superior performance.

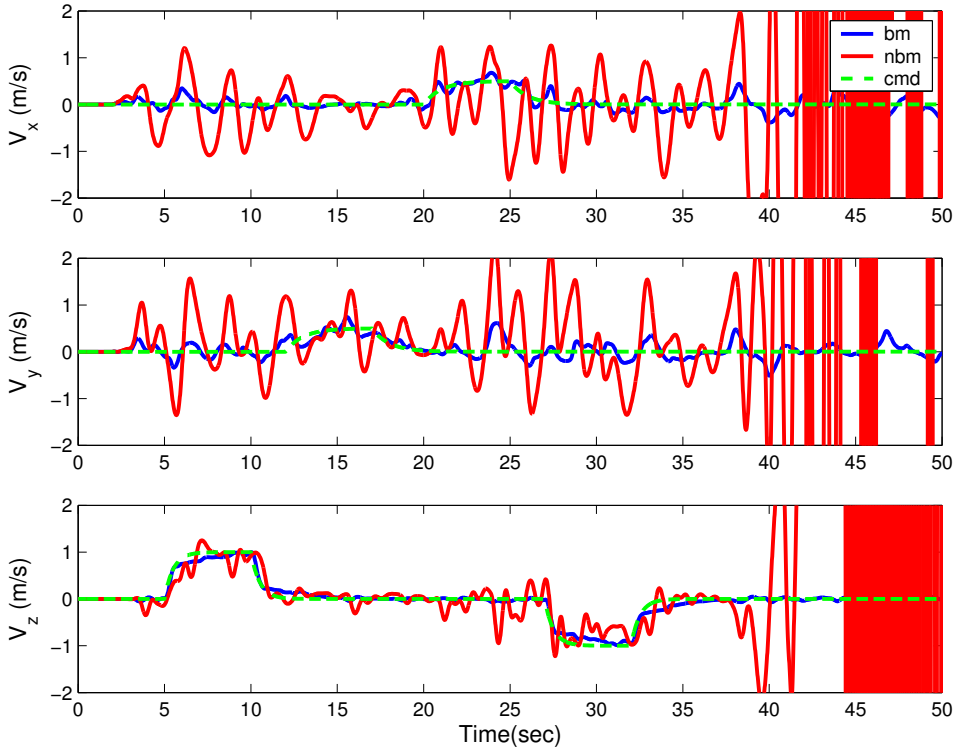

Figure 19: Vehicle translational velocity response during trajectory tracking. BM Case (blue line), NBM Case (red line), Command (dashed green line.

The corresponding vane and fan actuator time histories during tracking are shown in Figures 21 and 22, respectively. The case with BM (blue line) clearly needs less vane and fan control activity but as observed earlier gives smaller velocity tracking errors.

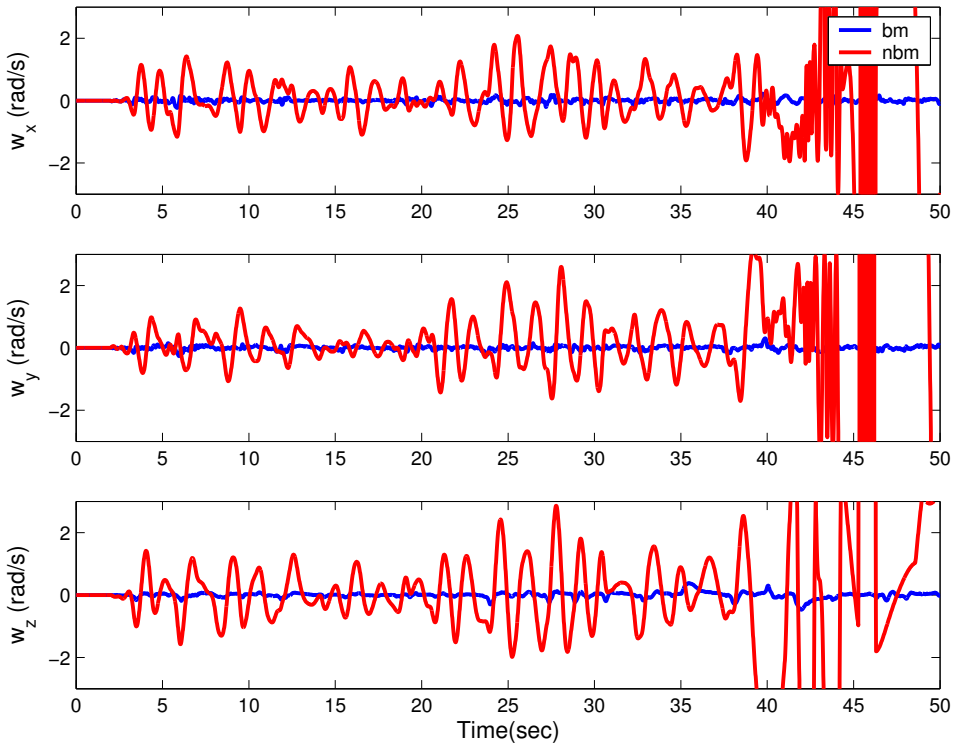

Figure 20: Vehicle angular velocity response during trajectory tracking. BM Case (blue line), NBM Case (red line).

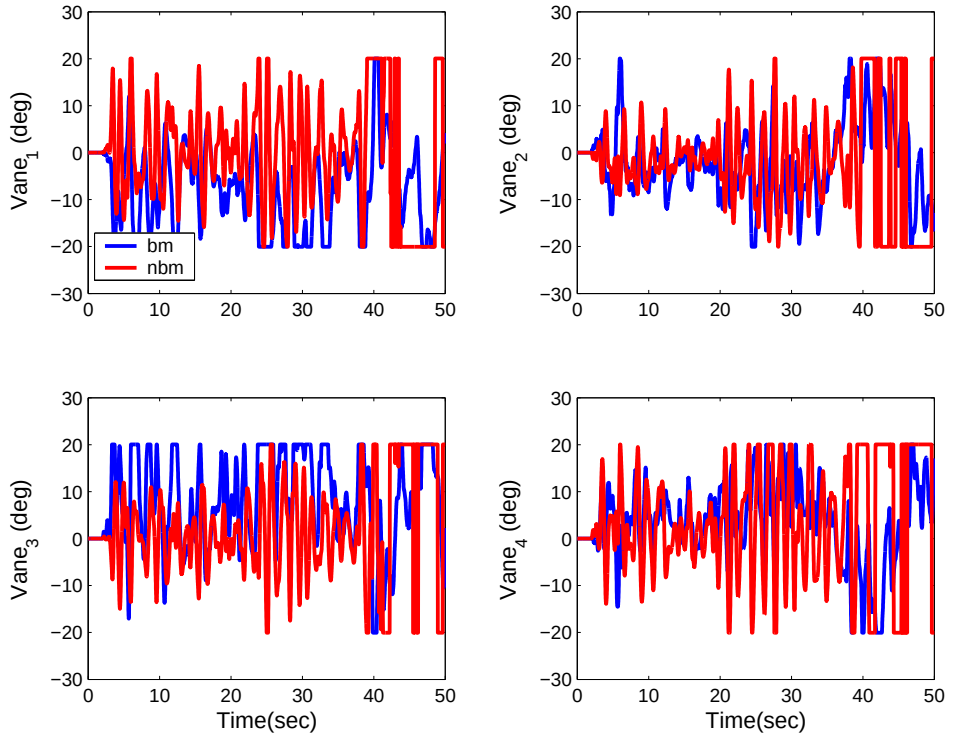

Figure 21: Vane angle response during tracking. BM Case (blue line), NBM Case (red line).

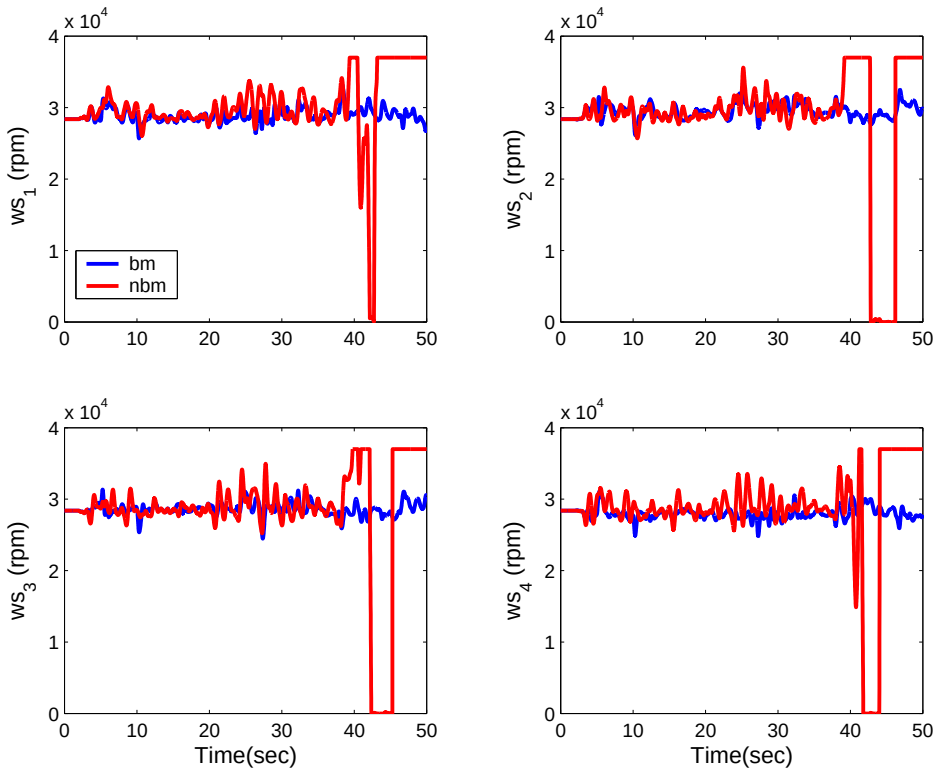

Figure 22: Fan speed response during command tracking. BM Case (blue line), NBM Case (red line).

7.5 Robustness to payload variations

7.5.1 Simulated Mass and Inertia changes.

To simulate variable payloads, assume a step increase of 20 % (3.36 kg) of the gross weight of the platform. A spherical uniformly distributed mass is assumed dropped at 0.15 m away from the center of mass location on the platform at 5 sec and is assumed to be dropped off (or removed) from the platform at 20 sec. The inertia matrix and total mass of the system is significantly changed as a result of the off-centered loading. This off-CG centered loading simulation is of particular interest due to its difficulty and its practical significance for a hovering platform where passengers or payloads can be loaded and unloaded with maximum flexibility without compromising vehicle stability while hovering. In this part of simulation, disturbances and measurement errors are not included to focus entirely on the effects of these payload changes.

7.5.2 Closed loop response during hover.

Figures 23 and 24 show the position and attitude responses to mass and inertia changes for both cases. It is seen that the platform position and attitude excursions are significantly better in the BM case as shown by the blue line.

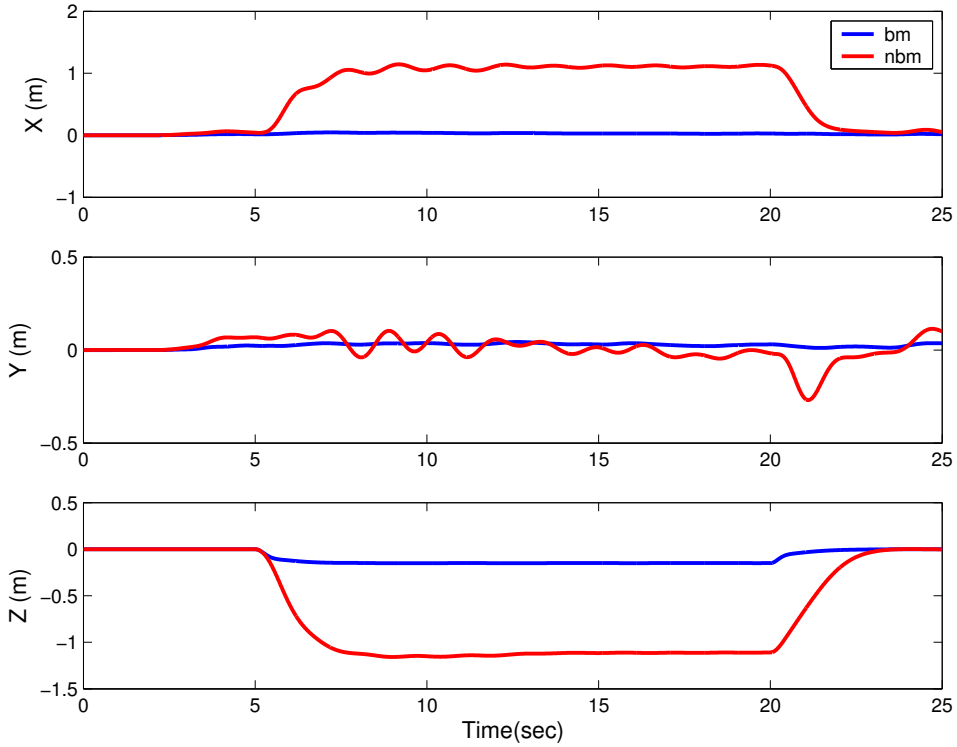

Figure 23: Position response to step changes in payload. BM Case (blue line), NBM Case (red line).

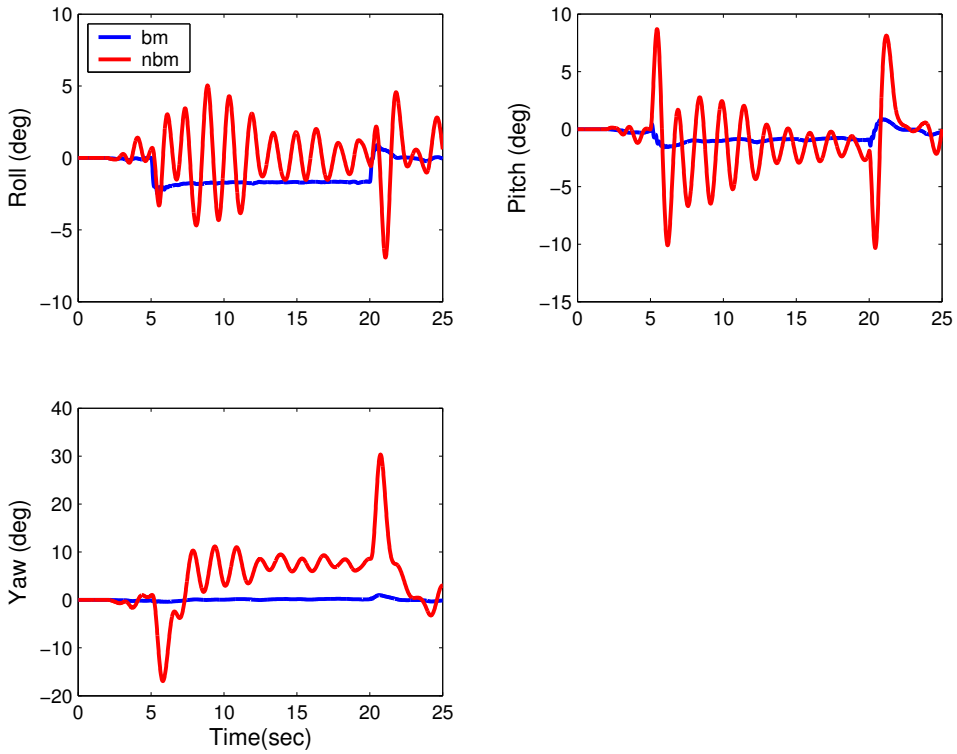

Figure 24: Attitude response to step changes in payload. BM Case (blue line), NBM Case (red line).

Significant differences are also noted in their corresponding vane and fan actuator histories as shown in Figures 25 and 26 respectively. It is seen that the fan speeds and vane angles oscillate significantly and rapidly in the NBM case resulting in the platform oscillations shown previously. Unfortunately, the actual consequences on flight performance due to this apparently more unsteady control vane activity for the NBM case, remains to be verified during an actual flight because a reliable mathematical model is not available for this class of unsteady aerodynamics.

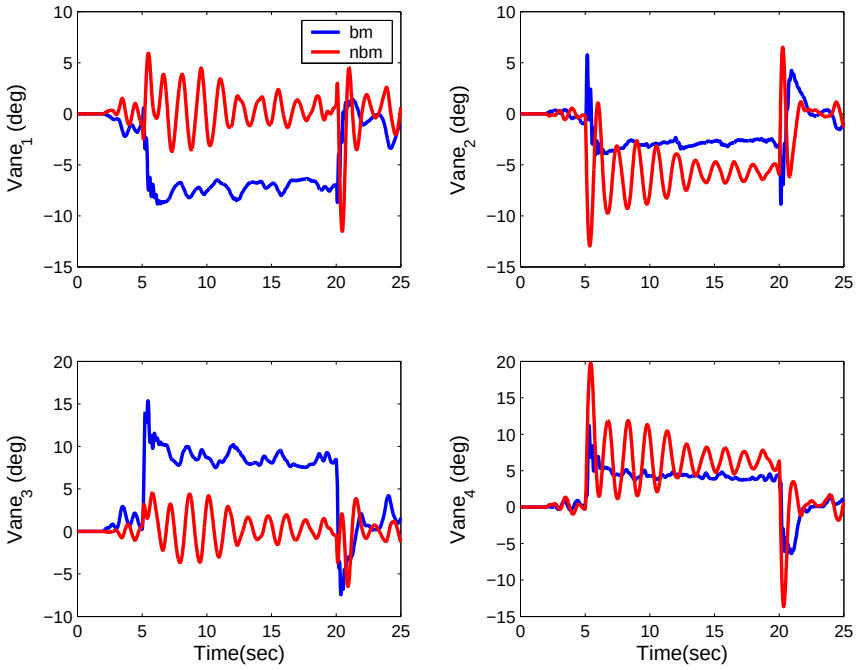

Figure 25: Control vane responses to step changes in payload. BM Case (blue line), NBM Case (red line).

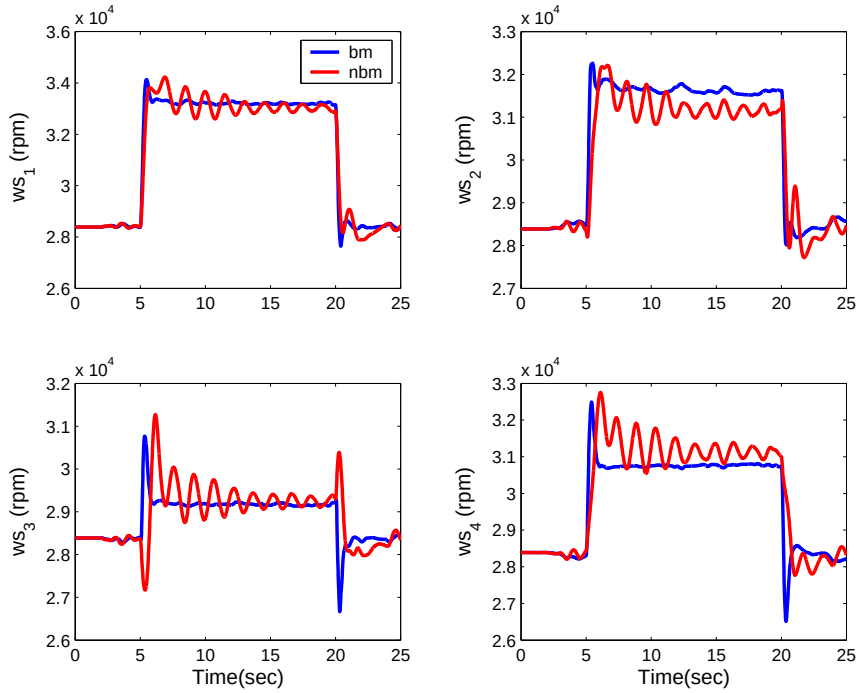

Figure 26: Fan speed responses to step changes in payload. BM Case (blue line), NBM Case (red line).

7.6 Summary of Simulation Results

Simulation results demonstrate the potential performance of a new stability and control technology, based on trying to mitigate control surface actuator induced unsteady aerodynamics effects in feedback control. Its ultimate goal is to enable statically unstable, disturbance sensitive, thrust levitated, low-speed or hovering vehicles to operate more safely than is possible today, in turbulent conditions and under large payload variations. Simulation results indicate that generic VTOL platforms can be endowed with significant directional stability with a proper amount of bias momentum, similar to a dual-spin stabilized spacecraft but under a significantly different operating environment. The results also indicate that this open loop directional stability carries over to closed loop if the controllers are designed properly. Specifically, it was found that vehicle attitude control robustness can be significantly improved (over a no-bias-momentum vehicle) during hovering, particularly under strong turbulent winds or significant payload variations. In addition, command tracking performance at low airspeeds can also be improved significantly particularly under turbulent winds, despite the presence of somewhat complicated gyroscopic coupling. These performance improvements are due to control laws that are based on proper modeling of the system dynamics. These predicted improvements in robustness obtained from detailed simulation studies are expected to be more evident during actual flight test, with the physical presence of control induced unsteady aerodynamics.

8 Conclusions

A new methodical approach to sizing bias momentum for dual spin hovering vehicles has been proposed which is based on the roll and pitch responses to disturbances. The approach is heuristic in nature and addresses a very practical but fundamental issue of bias momentum sizing for passive gyroscopic stability and the influence of the major factors including the assumed disturbance environment, nominal vehicle rotational inertia, and the designed level of attitude response of the vehicle to disturbances. Further work on realizing hardware system for storing a large amount of bias angular momentum is recommended. Clearly more detailed tradeoff and optimization in the design of momentum wheels tailored for air vehicles are also needed to improve performance further. Although spin stabilization is an established technology in spacecraft attitude control, flight validation is strongly recommended due to the vastly different operational environment faced by air vehicles.

Appendix

Indefinite integrals used:

$$\int \frac{dx}{(a^2-x^2)^2} = \frac{x}{2a^2(a^2-x^2)} + \frac{1}{4a^3}\ln\left(\frac{a+x}{a-x}\right) \tag{8.1}$$

$$\int \frac{x^2dx}{(a^2-x^2)^2} = \frac{x}{2(a^2-x^2)} - \frac{1}{4a^3}\ln\left(\frac{a+x}{a-x}\right) \tag{8.2}$$

$$\begin{aligned}\int \frac{dx}{(ax^2+bx+c)(ax^2-bx+c)} &= \frac{1}{4cb}[\ln(ax^2+bx+c) - \ln(ax^2-bx+c)] \\ &+ \frac{1}{2c\sqrt{4ca-b^2}}[\tan^{-1}\left(\frac{2ax-b}{\sqrt{4ca-b^2}}\right) \\ &+ \tan^{-1}\left(\frac{2ax+b}{\sqrt{4ca-b^2}}\right)]\end{aligned} \tag{8.3}$$

$$\begin{aligned}\int \frac{x^2dx}{(ax^2+bx+c)(ax^2-bx+c)} &= \frac{1}{4ba}[\ln(ax^2-bx+c) - \ln(ax^2+bx+c)] \\ &+ \frac{1}{2a\sqrt{4ca-b^2}}[\tan^{-1}\left(\frac{2ax-b}{\sqrt{4ca-b^2}}\right) \\ &+ \tan^{-1}\left(\frac{2ax+b}{\sqrt{4ca-b^2}}\right)]\end{aligned} \tag{8.4}$$

Taylor series of $\tan^{-1} x$ is

$$\tan^{-1} x = \begin{cases} x - \frac{x^3}{3} + \frac{x^5}{5} - \frac{x^7}{7} + \dots & |x| < 1 \\ \pm\frac{\pi}{2} - \frac{1}{x} + \frac{1}{3x^3} - \frac{1}{5x^5} + \dots & +\text{if} \quad 1 \le x, \quad -\text{if} \quad x \le -1 \end{cases} \tag{8.5}$$

References

[1] Fleming, J., Jones, T., Lusardi, J., Gelhausen, P., and Enns, D., "Improved control of ducted fan VTOL UAVs in crosswind turbulence," *4th AHS Decennial Specialists Conference on Aeromechanics*, San Francisco, California, January 21-23, 2004.

[2] Fleming, J., Jones, T., Gelhausen, P., and Enns, D., "Improving control system effectiveness for ducted fan VTOL UAVs operating in crosswinds", 2nd AIAA *Unmanned Unlimited* Systems, Technologies, and Operations - Aerospace, September 15-18, 2003, San Diego, California, AIAA Paper 2003-6514.

[3] Armutcuoglu, O., Kavsaoglu, M.S., and Tekinalp, O., "Tilt duct vertical takeoff and landing uninhabited aerial vehicle concept design study," *Journal of Aircraft*, Vol. 41, No. 2, March-April 2004, pp. 215-223.

[4] Hamel, T., Mahony, R., Lozano, R., and Ostrowski, J., *15 th Triennial World Congress*, Barcelona, Spain, 2002.

[5] http://dmaerosafe.freeservers.com/ homepage for DM AeroPlatforms Ltd.

[6] http://www.urbanaero.com/

[7] http://www.moller.com/skycar/m400/

[8] http://www.airscooter.com/

[9] *Spacecraft Attitude Determination and Control*, Edited by James R. Wertz, Kluwer, 1995.

[10] Kaplan, M.H., *Modern Spacecraft Dynamics & Control*, John Wiley & Sons, Inc., New York, 1976.

[11] Hughes, P.C., *Spacecraft Attitude Dynamics*, John Wiley & Sons, Inc., New York, 1986.

[12] Greenwood, D. T., *Principles of Dynamics*, Prentice-Hall Inc., Englewood-Cliffs, New Jersey, 1965, Chapter 8.

[13] Meirovitch, L., *Methods of Analytical Dynamics*, McGraw-Hill, Inc., New York, 1970.

[14] Chobotov, V.A., *Spacecraft Attitude Dynamics and Control*, Krieger Publishing Company, Malabar, Florida, 1991, p. 19-.

[15] Schilling, R.J., and Lee, H., *Engineering Analysis: A Vector Space Analysis*, John Wiley & Sons, New York, 1988.

[16] Skogestad, S., and Postlethwaite, I., *Multivariable Feedback Control: Analysis and Design*, John Wiley & Sons, Inc., New York, 1997, Appendix A.5.

[17] Hoblit, F.M., *Gust Loads on Aircraft: Concepts and Applications*, AIAA Inc, Washington D.C., 1988, Chapter 4.

[18] Newland, D.E., *Random vibrations and spectral analysis*, Longman, Inc., New York, 1975, page 73-.

[19] Lim,K.B., Shin,J.Y., Cooper, E.G., Moerder, D.D., Khong, T.H., and Smith,M.F., "An overview of the NASA Flying Test Platform research", AIAA Guidance, Navigation, and Control Conference and Exhibit, August 11-14, 2003, Austin, Texas. AIAA Paper 2003-5775.

[20] Lim,K.B., Shin,J.Y., Cooper, E.G., and Moerder, D.D., "A new approach to attitude stability and control for low airspeed vehicles", AIAA Guidance, Navigation, and Control Conference and Exhibit, August 16-19, 2004, Providence, RI. AIAA Paper 2004-5008.

[21] Lim,K.B., Shin,J.Y., and Moerder, D.D., "Bias momentum sizing for hovering dual-spin platforms," AIAA Guidance, Navigation, and Control Conference and Exhibit, August 15-18, 2005, San Francisco, CA. AIAA Paper 2005-5973.

[22] George H. Saunders, *Dynamics of Helicopter Flight*, John Wiley & Sons, Inc, New York, 1974.

[23] Prouty, R.W., *Helicopter Aerodynamics*, Vols. I-III, PJS Publications Inc, Peoria, Ill, 1985-1993.

[24] Army Aerial & Joint Services VTOL Rotorcraft Government/Industry/Academia Workshop, ASSP-2004, Williamsburg, Virginia, 27-29 January 2004.

[25] Schlichting, H., *Boundary Layer Theory*, McGraw-Hill, New York, 1979 (7th edition), p. 19.

REPORT DOCUMENTATION PAGE

Form Approved
OMB No. 0704-0188

1. REPORT DATE *(DD-MM-YYYY)*	2. REPORT TYPE	3. DATES COVERED *(From - To)*
01- 05 - 2006	Technical Publication	

4. TITLE AND SUBTITLE

Bias Momentum Sizing for Hovering Dual-Spin Platforms

5a. CONTRACT NUMBER

5b. GRANT NUMBER

5c. PROGRAM ELEMENT NUMBER

6. AUTHOR(S)

Lim, Kyong B.; Shin, Jong-Yeob; and Moerder, Daniel D.

5d. PROJECT NUMBER

5e. TASK NUMBER

5f. WORK UNIT NUMBER

23-561581.02.08

7. PERFORMING ORGANIZATION NAME(S) AND ADDRESS(ES)

NASA Langley Research Center
Hampton, VA 23681-2199

8. PERFORMING ORGANIZATION REPORT NUMBER

L-19257

9. SPONSORING/MONITORING AGENCY NAME(S) AND ADDRESS(ES)

National Aeronautics and Space Administration
Washington, DC 20546-0001

10. SPONSOR/MONITOR'S ACRONYM(S)

NASA

11. SPONSOR/MONITOR'S REPORT NUMBER(S)

NASA/TP-2006-214317

12. DISTRIBUTION/AVAILABILITY STATEMENT

Unclassified - Unlimited
Subject Category 08
Availability: NASA CASI (301) 621-0390

13. SUPPLEMENTARY NOTES

An electronic version can be found at http://ntrs.nasa.gov

14. ABSTRACT

An atmospheric flight vehicle in hover is typically controlled by varying its thrust vector. Achieving both levitation and attitude control with the propulsion system places considerable demands on it for agility and precision, particularly if the vehicle is statically unstable, or nearly so. These demands can be relaxed by introducing an appropriately sized angular momentum bias aligned with the vehicle's yaw axis, thus providing an additional margin of attitude stability about the roll and pitch axes. This paper describes a methodical approach for trading off angular momentum bias level needed with desired levels of vehicle response due to the design disturbance environment given a vehicle's physical parameters. It also describes several simplifications that provide a more physical and intuitive understanding of dual-spin dynamics for hovering atmospheric vehicles. This approach also mitigates the need for control torques and inadvertent actuator saturation difficulties in trying to stabilize a vehicle via control torques produced by unsteady aerodynamics, thrust vectoring, and unsteady throttling. Simulation results, based on a subscale laboratory test flying platform, demonstrate significant improvements in the attitude control robustness of the vehicle with respect to both wind disturbances and off-center of gravity payload changes during flight.

15. SUBJECT TERMS

Momentum bias sizing; Dual-spin; Hovering; Attitude control; Momentum wheel; Stability augmentation

16. SECURITY CLASSIFICATION OF:			17. LIMITATION OF ABSTRACT	18. NUMBER OF PAGES	19a. NAME OF RESPONSIBLE PERSON
a. REPORT	b. ABSTRACT	c. THIS PAGE			STI Help Desk (email: help@sti.nasa.gov)
					19b. TELEPHONE NUMBER *(Include area code)*
U	U	U	UU	53	(301) 621-0390